Pitch angle scattering of sub-MeV relativistic electrons by electromagnetic ion cyclotron waves

R. E. Denton [1], L. Ofman[2,3], Y. Y. Shprits [4,5,6], J. Bortnik [6], R. M. Millan [1], C. J. Rodger [7], C. L. da Silva [8], B. N. Rogers [1], M. K. Hudson [1], K. Liu [9], K. Min [10], A. Glocer[3], and C. Komar[2,3]

[1]Department of Physics and Astronomy, Dartmouth College, Hanover, New Hampshire, USA
[2]Department of Physics, Catholic University of America, Washington, District of Columbia, 20064, USA.
[3]NASA GSFC, Code 673, Greenbelt, Maryland, 20771, USA.
[4]GFZ German Research Center for the Geosciences, Helmholtz Center Potsdam, Potsdam, Germany
[5]University of Potsdam, Institute for Physics and Astronomy, Potsdam, Germany
[6]Department of Atmospheric and Oceanic Sciences, University Of California at Los Angeles, Los Angeles, California, USA
[7]Department of Physics, University of Otago, Dunedin, New Zealand.
[8]Department of Physics and Langmuir Laboratory, New Mexico Institute of Mining and Technology, Socorro, New Mexico, 87801, USA.
[9]Southern University of Science and Technology, Shenzhen, Guangdong, China.
[10]Korea Astronomy and Space Science Institute, Daejeon 34055, Republic of Korea.

Corresponding author: R. E. Denton, `redenton at dartmouth dot edu`

Abstract

Electromagnetic ion cyclotron (EMIC) waves have long been considered to be a significant loss mechanism for relativistic electrons. This has most often been attributed to resonant interactions with the highest amplitude waves. But recent observations have suggested that the dominant energy of electrons precipitated to the atmosphere may often be relatively low, less than 1 MeV, whereas the minimum resonant energy of the highest amplitude waves is often greater than 2 MeV. Here we use relativistic electron test particle simulations in the wave fields of a hybrid code simulation of EMIC waves in dipole geometry in order to show that significant pitch angle scattering can occur due to interaction with low amplitude short wavelength EMIC waves. In the case we examined, these waves are in the H band (at frequencies above the He+ gyrofrequency), even though the highest amplitude waves were in the He band frequency range (below the He+ gyrofrequency). We also present wave power distributions for 29 EMIC simulations in straight magnetic field line geometry that show that the high wave number portion of the spectrum is in every case mostly due to the H band waves. Though He band waves are often associated with relativistic electron precipitation, it is possible that the He band waves do not directly scatter the sub-MeV electrons, but that the presence of He band waves is associated with high plasma density which lowers the minimum resonant energy so that these electrons can more easily resonate with the H band waves.

1 Introduction

EMIC waves can cause pitch angle scattering of relativistic electrons and consequent precipitation into the ionosphere. This mechanism has been considered by some researchers to be an important loss mechanism for radiation belt electrons [*Shprits et al.*, 2008; *Millan and Thorne*, 2007]. Recent experimental results include simultaneous observation of EMIC waves and relativistic electron precipitation [*Miyoshi et al.*, 2008; *Kersten et al.*, 2014; *Li et al.*, 2014; *Hyun et al.*, 2014; *Blum et al.*, 2015; *Clilverd et al.*, 2015; *Rodger et al.*, 2015; *Zhang et al.*, 2016].

Electromagnetic ion cyclotron (EMIC) waves occur in the vicinity of the ion gyrofrequencies, and so are strongly affected by the concentration of heavy ions. In a plasma consisting of H+, He+, and O+, there are three left-hand polarized wave bands which asymptote up in frequency to the gyrofrequency of the corresponding ion, the H band, He band, and O band. So the H band occurs at frequencies above the He+ gyrofrequency, and asymptotes up toward the H+ gyrofrequency. Because of “crossover frequencies”, where the polarization of the waves switches between left and right hand polarized, the actual topology of the surfaces can be quite complicated; see the descriptions by *Andre* [1985], *Hu et al.* [2010], and especially by *Hu* [2010]. But for our purposes, it will suffice to consider there to be three left-hand polarized wave surfaces on which the EMIC waves grow. Usually the waves are generated near the magnetic equator, where the magnetic field has a minimum value and hence the plasma beta has maximum value. The waves refract as they convect away from the magnetic equator along magnetic field lines, and the polarization turns linear [*Denton*, 2018].

Left-hand polarized EMIC waves resonate predominantly with low pitch angle relativistic electrons [*Summers et al.*, 2007a,b], producing characteristic pitch angles distributions with clear bite-outs at smaller pitch angles. That is, the particles with large pitch angle are less affected, so that at relatively low energies (up to about 1 or 2 MeV), the bulk of the distribution function may be relatively unaffected [*Usanova et al.*, 2014; though see *Aseev et al.*, 2017]. In some cases, transport by higher-frequency whistler mode hiss or chorus waves, in combination with EMIC waves, can help facilitate decrease in the distribution function at all pitch angles [*Li et al.*, 2007; *Shprits et al.*, 2009, 2017, 2018; *Aseev et al.*, 2017]. But the simulations we will be using to examine pitch angle scattering do not include the high-frequency waves, so the pitch angle scattering studied in this paper results entirely from the EMIC waves.

In quasi-linear diffusion theory, only the electrons in resonance will be strongly affected by pitch angle scattering. The resonance condition is

$$\omega - k_{\|} V_{\|} = -n \frac{\Omega_{\mathrm{ce}}}{\gamma}, \tag{1}$$

where ω is the wave frequency; $k_{\|}$ is the component of the wave vector parallel to the background magnetic field; $V_{\|}$ is the parallel component of the relativistic electron velocity V; n is the order of the resonance; $\Omega_{\mathrm{ce}} = eB/m_{\mathrm{e}}$ is the nonrelativistic electron cyclotron frequency, where e is the absolute value of the electron charge, B is the background magnetic field, and m_{e} is the electron rest mass; and $\gamma = 1/\sqrt{1-(V/c)^2}$ is the relativistic factor for the electron [*Kennel and Petschek*, 1966; *Shprits et al.*, 2008; *Albert and Bortnik*, 2009]. For resonance with EMIC waves [*Cornwall*, 1965; *Kennel and Petschek*, 1966; *Meredith et al.*, 2003; *Denton et al.*, 2014, 2015; *Li et al.*, 2014], the lowest energy interaction with relativistic electron occurs for $n = 1$.

Considering that EMIC waves are at frequency below the proton gyrofrequency, we can neglect the ω term and get

$$k_{\|}V_{\|} = \frac{\Omega_{\rm ce}}{\gamma}. \tag{2}$$

Equation (2) makes it clear that it is $k_{\|}$ along with $\Omega_{\rm ce} \sim B$, rather than ω, that are important for pitch angle scattering of relativistic electrons. (Time variation on timescales longer than ω^{-1} can lead to changes in both $k_{\|}$ and $\Omega_{\rm ce}$.) Higher $k_{\|}$ results in lower resonant energies. Note that increased plasma density causes EMIC waves to have lower phase velocity, and hence larger $k_{\|}$ (for the relatively fixed frequencies of EMIC waves just below the ion gyrofrequencies). The EMIC dispersion relation involves the normalized $k_{\|}$ value, $k_{\|}c/\omega_{\rm pp}$ [*Denton et al.*, 2015], where c is the speed of light and $\omega_{\rm pp} \equiv \sqrt{N_{\rm e}e^2/(m_{\rm p}\epsilon_0)}$ is the plasma frequency using the electron density, $N_{\rm e}$, and proton mass, $m_{\rm p}$, where e is the electron charge, and ϵ_0 is the permittivity of free space. Since $\omega_{\rm pp} \propto N_{\rm e}^{0.5}$, large density can lead to large unnormalized $k_{\|}$.

A statistical study showed that for most EMIC events the resonant energy was above 2 MeV [*Meredith et al.*, 2003]. *Meredith et al.* [2003] argued that the minimum resonant energy could drop as low as 500 keV when the total density was large, such as might occur in the plasmasphere or a plasmaspheric plume. And *Ukhorskiy et al.* [2010] suggested that the finite width of the frequency spectrum could greatly decrease the minimum resonant energies for interaction with He band EMIC waves. But both of these studies used the cold plasma dispersion relation, which may not be valid. Note that Figure 1f of *Denton* [2018], reproduced in Figure 3c and showing the warm plasma dispersion relation for a case that we will examine in detail, indicates that the high wave number portion of the He band (missing in the figure) is damped.

Observations indicate, however, that significant precipitation due to EMIC waves can occur even at energies as low as 300 keV [*Millan et al.*, 2007; *Zhang et al.*, 2016; *Hendry et al.*, 2017, and references therein]. If ultra-relativistic (several MeV) electrons are much more greatly affected by EMIC waves than sub-MeV relativistic electrons, why is it that the dominant precipitation energy is often only hundreds of keV [*Hendry et al.*, 2017]? And if the dominant precipitation of relativistic electrons is at sub-MeV energies, how could it be that the equatorial pitch angle distribution of the sub-MeV particles is sometimes relatively unaffected [*Usanova et al.*, 2014]? *Rodger et al.* [2018] recently suggested a possible solution, that EMIC waves do cause precipitation of sub-MeV relativistic electrons, but the sub-MeV precipitated electrons are only a small fraction of the equatorial distribution. Even though ultra-relativistic (several MeV) electrons are much more strongly affected by EMIC waves, there are very few of these particles compared to the sub-MeV population. So the sub-MeV relativistic electrons dominate the observed precipitation.

The question still arises, however, as to why sub-MeV relativistic electrons are affected at all by EMIC waves, since they may not be in resonance with the waves. This paper addresses that question. We will show that relativistic electrons can be pitch angle scattered by low amplitude EMIC waves with larger parallel wave number ($k_\parallel$) than the highest amplitude waves. Furthermore, we find that these larger $k_\parallel$ waves are likely to be in the EMIC H band, even if the highest amplitude waves are in the He band. This suggests that the process leading to precipitation of sub-MeV relativistic electrons may be much more complex than has been supposed.

In section 2, we use the wave fields of a recent simulation of EMIC waves in dipole geometry [*Denton*, 2018] to show that sub-MeV (as well as high energy) relativistic electrons can be affected by EMIC waves, but that the waves that scatter the sub-MeV particles are low amplitude high $k_\parallel$ H band EMIC waves. We also investigate the origin of the high $k_\parallel$ waves. In section 3, we use a recent series of EMIC simulations in straight field geometry [*Ofman et al.*, 2017] to show that high $k_\parallel$ waves are likely to be in the EMIC H band for a wide range of parameters. And in section 4, we summarize the results of this paper.

2 Pitch angle scattering of relativistic electrons by EMIC waves in dipole geometry

We will investigate the pitch angle scattering of test particle relativistic electrons in the fields produced from a hybrid code simulation of EMIC waves in dipole geometry.

2.1 Description of simulation fields

For this part of our study, we use the simulation wave fields of *Denton* [2018]. As described by Denton, the waves were driven by an initially anisotropic population of hot protons with parallel plasma beta (based on the parallel pressure) of 0.403 and perpendicular to parallel temperature ratio of 2. The concentration of hot protons, cold protons, cold helium, and cold oxygen were respectively 0.033, 0.92, 0.03, and 0.017 (see Table 1 of *Denton* [2018]). With these parameters, the plasma was very unstable, although not beyond the range of realistic conditions. *Denton* [2018] used a large number of particles, smoothing, and filtering in Fourier space in order to eliminate spatial power at the grid scale.

We use the wave fields around 90 s into the simulation of *Denton* [2018]. The transverse wave magnetic field components are shown in Figure 1 in the L direction perpendicular to the equilibrium field and radially outward (Figure 1a) and azimuthal direction s into the page (Figure 1b). (These plots are the same as Figure 3Ca and 3Cb of *Denton* [2018].) The field components are plotted versus the curvilinear coordinates q and L shell. The parallel coordinate q varies from 0 at the magnetic equator to 1 at the northern boundary of the simulation, which is at 47°on the central field line at $L = 6.6$ (roughly geostationary orbit). The roughly vertical curves in Figure 1a and 1b show that field line. To relate this to magnetic latitude MLAT, the values of MLAT at the largest L value are shown to the right of Figure 1b and the roughly horizontal green curves are drawn at MLAT values of 10°, 20°, 30°, and 40°. For the test particle simulations, we use the time dependent total magnetic field around this time, and also include the electric field (not shown). As we will show, the electric field has a negligible effect on the pitch angle scattering of relativistic electrons.

2.2 Pitch angle diffusion

The pitch angle α of a particle is the angle between a particle's velocity and the magnetic field. Because α varies adiabatically along the field line, it is helpful to consider the equatorial pitch angle, α_0. This is found from the local and equatorial magnetic field values, assuming $p_\perp^2 \propto B$ to conserve the first adiabatic invariant, where $p_\perp$is the particle momentum for motion perpendicular to the magnetic field.

We initialize 4.7 million relativistic electron test particles between $L = 6.4$ and 6.8 in the fields of Figure 1a and 1b with energies between 0 and 10 MeV, and run the simulation for 0.1 s. The use of test particles to represent relativistic electrons is reasonable, since the plasma pressure of this population is negligible. The particles are initially placed at positions along the field line in proportion to the density of an equilibrium distribution. Using the changes in the equatorial pitch angle of the test particles, we plot in Figure 1c the base 10 logarithm of the diffusion coefficient of the equatorial pitch angle in bins of the initial energy and equatorial pitch angle. For each bin, the diffusion coefficient

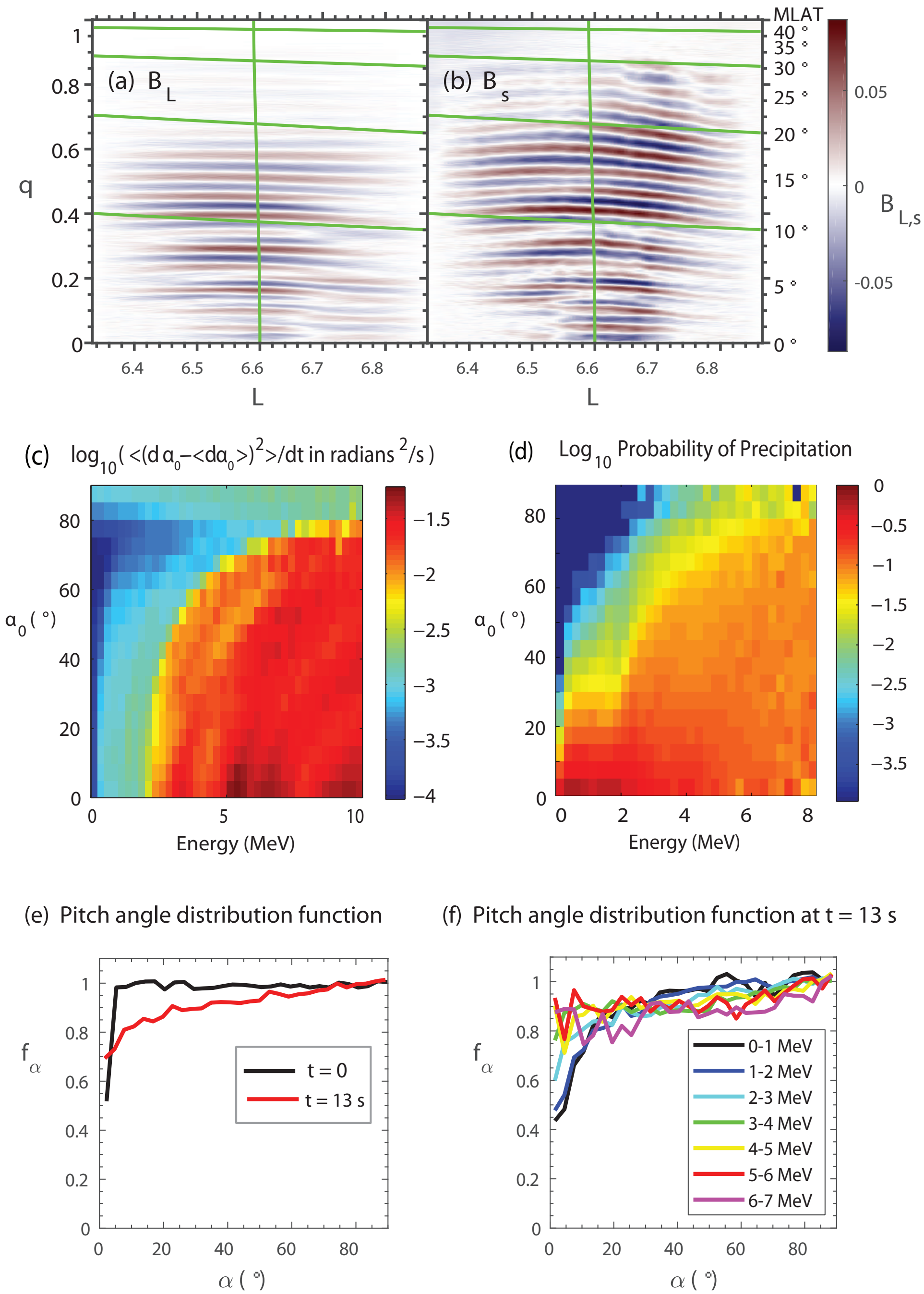

Figure 1. Statistical results for pitch angle scattering in hybrid simulation fields. (a) L component of the magnetic field, B_L, and (b) s component of the magnetic field, B_s at $t = 90$ s; (c) base 10 log of the equatorial pitch angle diffusion coefficient (color) at $t = 90$ s in radians^2/s versus energy on the horizontal scale and equatorial pitch angle on the vertical scale; (d) base 10 log of the probability of precipitation in 13 s roughly centered on $t = 90$ s versus energy and equatorial pitch angle; (e) for all particle energies, initial normalized pitch angle distribution (black curve) and the distribution after 13 s (red curve); (f) normalized pitch angle distribution after 13 s for the energy ranges indicated in the legend.

is $\left\langle (d\alpha_0 - < d\alpha_0 >)^2 \right\rangle / (2\Delta t)$, where $\langle\rangle$ indicates an average over the particles that start out in each bin, and $\Delta t = 0.1$ s. For this event, the minimum resonant energy for interaction with the highest amplitude waves on the central field line (with crest to crest wavelength evident in Figures 1a and 1b) is about 4 MeV. While the diffusion is certainly largest for energies greater than approximately 2.5 MeV, the diffusion coefficient is also significantly large at smaller energies. (The fact that the largest diffusion in Figure 1c extends down to 2.5 MeV may be because of resonance with particles in regions other than the central L shell at the equator.) The very steep dropoff in the diffusion in energies below 0.25 MeV is due to our Fourier space filtering of the magnetic field.

2.3 Precipitation of particles

Normally particles in our simulation reflect at the northern (high q or MLAT) boundary of the simulation. But each time a particle crosses that boundary, we check to see if the particle has a small enough pitch angle so that the particle could reach the atmosphere, assuming an adiabatic change in the perpendicular momentum. That is, we check to see if the particle is in the loss cone. If so, the particle is removed from the simulation, and we consider that it has "precipitated".

For the purposes of examining precipitation, we use a longer test particle simulations with a time interval of 13 s surrounding $t = 90$ s in the simulation of *Denton* [2018]. Figure 1d shows the base 10 logarithm of the probability of precipitation. In this plot, red color corresponds to a probability of precipitation of about 10% and orange color corresponds to a probability of precipitation of about 4%. So the probability of precipitation is quite large for most combinations of initial energy and equatorial pitch angle. The only exception is the upper left corner of the plot corresponding to low energy and large equatorial pitch angle.

Figure 1e shows the normalized pitch angle distribution for the 13 s simulation, averaging over particles with all energies, with the black curve representing the distribution function at the start of the simulation, and the red curve representing the distribution function at the end of the 13 s. To make this plot, we used only the particles in the region $q < 0.2$, corresponding to about MLAT $< 5°$ (Figure 1a and 1b). So this plot roughly shows the equatorial distribution function. The steep drop-off in the distribution function at small α_0 at the initial time occurs because we only initialized particles outside of the equatorial loss cone. Evidently there is a decrease of the particle distribution function at low pitch angles, whereas the distribution function at the largest pitch angles is not greatly affected.

Figure 1f also shows the normalized pitch angle distribution function at the end of the 13 s simulation, but now separated into different energy ranges. At the lowest energies, such as 0–1 MeV (black curve) and 1–2 MeV (dark blue curve), the pitch angle distribution is significantly reduced at low pitch angles, with a prominent loss cone feature still evident, and is relatively unaffected at pitch angles near 90°. But the behavior is quite different at the largest energies like 5–6 MeV (red curve) and 6–7 MeV (purple curve). These pitch angle distributions are reduced even for particles that start out close to $\alpha_0 = 90°$, and there is no prominent loss cone feature (precipitous drop in the distribution function at low pitch angles). A filled loss cone is thought to result from "strong scattering" that scatters particles into the loss cone as fast as they can be removed [*Kennel*, 1969].

Thus we see two different regimes of scattering. At the very high energies, above the minimum resonant energy for interaction with the highest amplitude waves, we see strong interaction that affects the pitch angle distribution up to, or at least up to a value close to, $\alpha_0 = 90°$. For particles with energy well below the minimum resonant energy for interaction with the highest amplitude waves, there is significant loss at small pitch angles, but little effect above about 50° (see Figure 1f).

2.4 Pitch angle scattering of a 0.55 MeV electron

We are most interested in the pitch angle scattering of the particles that have energy well below the minimum resonant energy of the highest amplitude waves. In this section we consider the motion of a single electron with kinetic energy 0.55 MeV during a time period of about 8 ms. Figure 2 shows a number of quantities related to the particle motion at this time. Within the 8 ms time interval, there are 12 gyroperiods of the particle motion, as can be seen from the oscillations in particle velocity (green curves) in Figures 2d–2g. Figure 2i shows the magnetic latitude, MLAT, which increases from 0° to about 3°. Figure 2h shows the normalized L coordinate, $r = L/6.6$ (so that $r = 1$ is at geostationary orbit). The value $r \sim 0.9983$ corresponds to $L = 6.588$, which is very close to the central field line of the simulation at $L = 6.6$. Figure 2a shows the pitch angle α (green

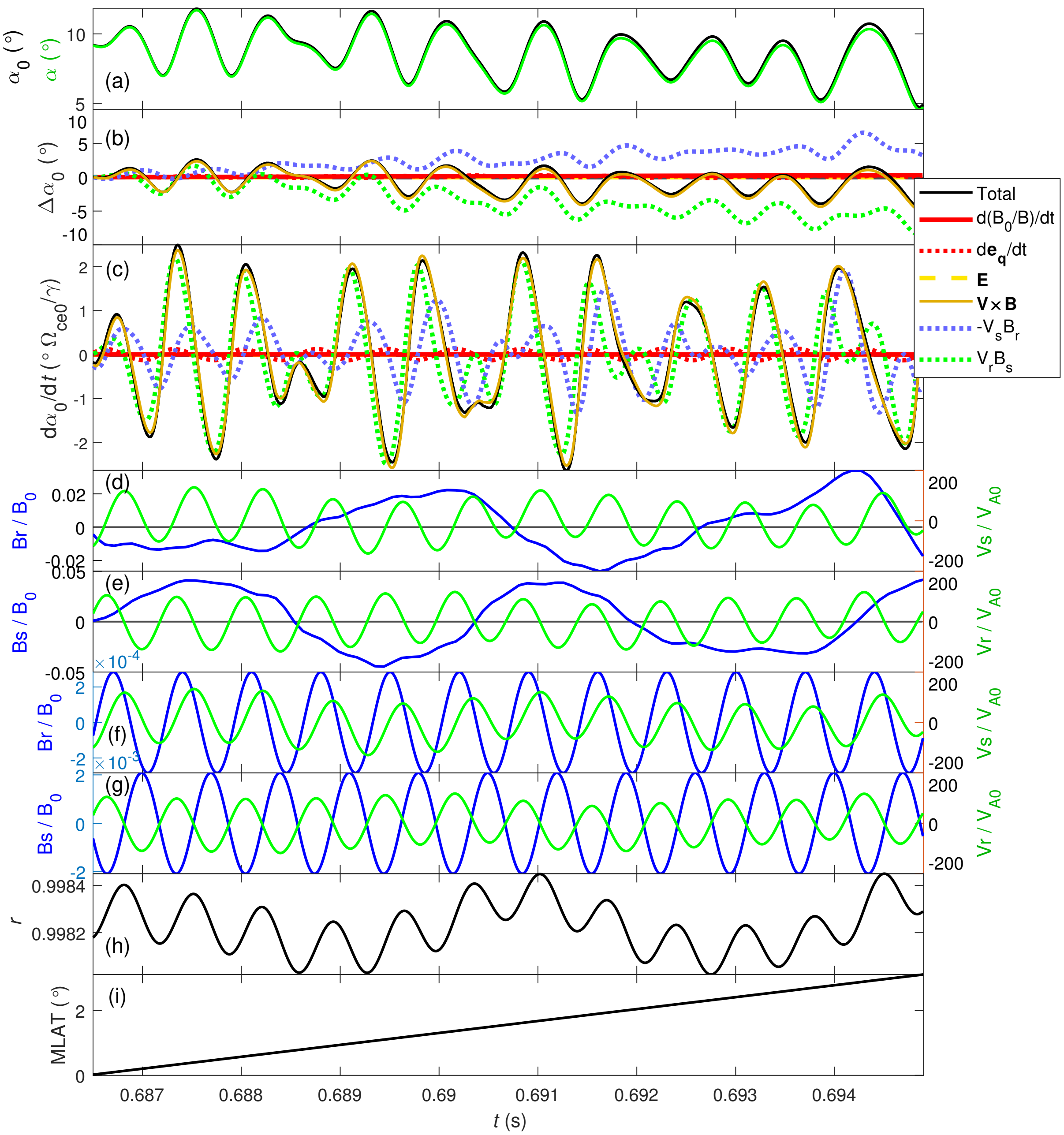

Figure 2. Properties of a 0.55 MeV electron experiencing pitch angle scattering. Versus time in s, (a) pitch angle α (green curve) and equatorial pitch angle α_0 (black curve); (b) Change in α_0 due to the terms indicated in the legend; (c) $d\alpha_0/dt$ due to the terms indicated in the legend; (d) radial magnetic field component B_r/B_0 (blue curve) and azimuthal particle velocity V_s/V_{A0} (green curve); (e) azimuthal magnetic field component B_s/B_0 (blue curve) and radial particle velocity V_r/V_{A0} (green curve); (f) and (g) same as (d) and (e) except that the magnetic field has been filtered to frequencies within 4% of the particle gyrofrequency; (h) normalized L shell coordinate r; (i) particle magnetic latitude MLAT.

curve) and equatorial pitch angle α_0 (black curve) versus time. These are nearly the same since this particle is very close to the magnetic equator (MLAT < 3°). During this time, the pitch angle averaged over a gyroperiod decreases by about 2.5°.

The black curve in Figure 2b shows the change in the equatorial pitch angle, $\Delta\alpha_0$. The other curves break down $\Delta\alpha_0$ into a number of parts. Defining $\mu_0' \equiv \sin^2\alpha_0$,

$$\frac{d\alpha_0}{dt} = \frac{1}{2\cos\alpha_0 \sin\alpha_0}\frac{d\mu_0'}{dt}. \tag{3}$$

Similarly, we define $\mu' \equiv \sin^2\alpha$. Then assuming conservation of the first adiabatic invariant, so that $U_{\perp 0}^2/B_0 = U_\perp^2/B$, where $\mathbf{U} = \gamma\mathbf{V}$ is the relativistic momentum divided by the particle rest mass, and the "0" subscript represents the value at the magnetic equator,

$$\frac{d\mu_0'}{dt} = \frac{d}{dt}\left(\frac{B_0}{B}\right)\mu' - 2\frac{B_0}{B}\cos\alpha\frac{d}{dt}(\cos\alpha). \tag{4}$$

Then from $\cos\alpha = U_\parallel/U$, we have

$$\frac{d\cos\alpha}{dt} = \frac{1}{U}\left(\frac{dU_\parallel}{dt} - \frac{U_\parallel}{U}\frac{dU}{dt}\right). \tag{5}$$

Here we choose to work in the unmodified dipole coordinates, so that $U_\parallel = \mathbf{e}_q \cdot \mathbf{U}$, where $\mathbf{e}_q$ is the unit vector in the q direction along the dipole magnetic field. Then using the Lorentz force, $d\mathbf{U}/dt = (q/m)(\mathbf{E} + \mathbf{V}\times\mathbf{B})$, where q and m are the charge and mass of the particle,

$$\frac{d\cos\alpha}{dt} = \frac{1}{U}\left[\frac{d\mathbf{e}_q}{dt}\cdot\mathbf{U} + \mathbf{e}_q\cdot\frac{q}{m}(\mathbf{E} + \mathbf{V}\times\mathbf{B}_\perp) - \frac{U_\parallel}{U}\mathbf{U}\cdot\frac{q}{m}\mathbf{E}\right], \tag{6}$$

where $\mathbf{B}_\perp$ is perpendicular to $\mathbf{e}_q$. Evidently there is a term proportional to $d(B_0/B)/dt$ in (4), and in (6) terms proportional to $d\mathbf{e}_q/dt$, $\mathbf{E}$, and $\mathbf{V}\times\mathbf{B}_\perp$, where $\perp$ indicates directions perpendicular to the dipole q direction, that is, in the r and s directions. Looking for the parallel acceleration that contributes to changes in the pitch angle, we can express the q component of $\mathbf{V}\times\mathbf{B}_\perp$ as the sum of two parts, $V_r B_s$ and $-V_s B_r$.

Figure 2b shows the contribution of each of these terms to the total change in the equatorial pitch angle (black curve) using the colors and line styles indicated in the legend. It is clear that all of the terms except for the one coming from $\mathbf{V}\times\mathbf{B}$ are negligible. (To the fast-moving electrons, the EMIC waves are an almost static magnetic structure.) Furthermore, it is the $V_r B_s$ term that is causing the decrease in the pitch angle. The $-V_s B_r$ term by itself is actually leading to increase. (We are not saying here that this is necessarily true for all particles.)

Figure 2c shows the contributions of all these terms to $d\alpha_0/dt$. The time derivative fluctuates greatly. Again, the only large terms come from $\mathbf{V} \times \mathbf{B}$.

Figures 2d and 2e respectively show B_r and B_s (blue curves) and V_s and V_r (green curves). It is immediately obvious that the oscillations in the particle velocity due to the gyromotion (oscillations in green curves) are not linked in phase to the large-scale oscillations of the magnetic field (oscillations in blue curves). There do seem to be some smaller amplitude fluctuations in the magnetic field, but it is difficult to see a consistent relationship between the phase of those fluctuations and the gyrophase.

Figures 2f and 2g are the same as Figures 2d and 2e, except that the magnetic field observed in the frame of the particle (with frequency on the left side of (1), roughly equal to the left side of (2)) has been band-passed filtered to allow only those frequencies within 4% of the gyrofrequency adjusted with the relativistic correction (right side of (2), and the frequency of oscillation in Figures 2f and 2g). From Figure 2g, it can be seen that V_r and B_s are exactly out of phase so that $V_r B_s$ is negative. Since the charge $-e$ of an electron is negative, the force $-eV_r B_s$ is in the positive q direction. Considering that the particle is moving in the positive q direction (Figure 2i), it is accelerated, leading to greater $V_{\|}$ and smaller pitch angle. Thus resonance with the wave field leads to the pitch angle scattering, but the resonance that causes the pitch angle scattering is with the small amplitude waves with frequency near the gyrofrequency.

Comparing the left side scales of the axes in Figures 2e and 2g, we see that the amplitude of the gyrofrequency oscillations of the magnetic field in Figure 2g is 25 times smaller than the highest amplitude fluctuations of the magnetic field in Figure 2e. That means that the wave energy of the oscillations interacting with the particle is 625 times smaller than the wave energy of the highest amplitude oscillations. This explains how particles with low energy can experience pitch angle scattering, and why that scattering is much less than the scattering at higher energies (Figures 1c, 1d, and 1f).

2.5 Properties of the waves that scattered the 0.55 MeV electron

Using the data repository of *Denton* [2018], we now examine the properties of the perpendicular wave magnetic field at around t = 90 s (80–100 s) at around MLAT = 2.6° (q = 0–0.2). Since the wave fields around t = 90 s were used in the test particle simulation, and the 0.55 MeV electron was scattered close to the magnetic equator, these are the fields most appropriate for understanding the pitch angle scattering of this electron. Figure 3a shows the perpendicular wave power versus $k_{\|}$. As indicated by (2), $k_{\|}$ is the crucial wave parameter that determines resonance with relativistic electrons. The curves in Figure 3a with black, cyan, and red color respectively show the wave power for H, He, and O band waves; solid and dotted curves show wave power propagating respectively earthward (away from the magnetic equator) or equatorward. For $k_{\|}c/\omega_{\text{pp}}$ above 0.25, the wave power in the H band (black curves) is dominant. The steep dropoff in wave power at $k_{\|}c/\omega_{\text{pp}} = 2.6$ is due to the Fourier space filtering mentioned previously. But that is well above the $k_{\|}$ value of the resonant wave for the 0.55 MeV electron (gray vertical line in Figure 3a).

We used the parallel velocity of the 0.55 MeV electron to convert the frequency range for bandpass filtering (used for Figures 2f and 2g) to a range of $k_{\|}$, $1.32 < k_{\|}c/\omega_{\text{pp}} < 1.43$. The value of $k_{\|}c/\omega_{\text{pp}}$ corresponding to the gyrofrequency was 1.38. The gray vertical line in Figure 3a is drawn at this value of $k_{\|}c/\omega_{\text{pp}}$, and Figure 3a shows that it is a factor of two below the value 2.6 used for the Fourier space filtering. At this value of $k_{\|}$, there are 8 grid points per wavelength. Below $k_{\|}c/\omega_{\text{pp}} = 1.3$, the perpendicular wave power in the H band is predominantly propagating earthward (solid black curve higher than the dotted black curve in Figure 3a to the left of the gray vertical line), whereas at $k_{\|}c/\omega_{\text{pp}} = 1.38$ and larger values of $k_{\|}$, the perpendicular wave power in the H band is about equal for that propagating earthward (black solid curve) or equatorward (black dotted curve).

Using the $k_{\|}$ bandpass filtered wave power ($1.32 < k_{\|}c/\omega_{\text{pp}} < 1.43$), we then plotted the perpendicular wave magnetic field power versus the wave frequency ω in Figure 3b. The wave power for this range of $k_{\|}$ is strongly left hand polarized (negative frequencies) and is concentrated in two peaks, one broader peak at $\omega/\Omega_{\text{cp}} = -0.4$ (labeled with a red asterisk), and one more narrow peak at $\omega/\Omega_{\text{cp}} = -0.8$ (labeled with a blue asterisk), both in the H band ($\left|\omega/\Omega_{\text{cp}}\right| > 0.25$). We verified that the waves in Figure 3b are approximately parallel propagating, as suggested by the strong left-hand polarization.

The fact that the waves are left hand polarized suggests that they are related to the EMIC waves. The largest peak in wave power at $\omega/\Omega_{\text{cp}} = -0.8$ (labeled with the blue asterisk), has somewhat more wave power propagating earthward then that propagating equatorward (blue curve higher than red curve). This might suggest that this wave power was

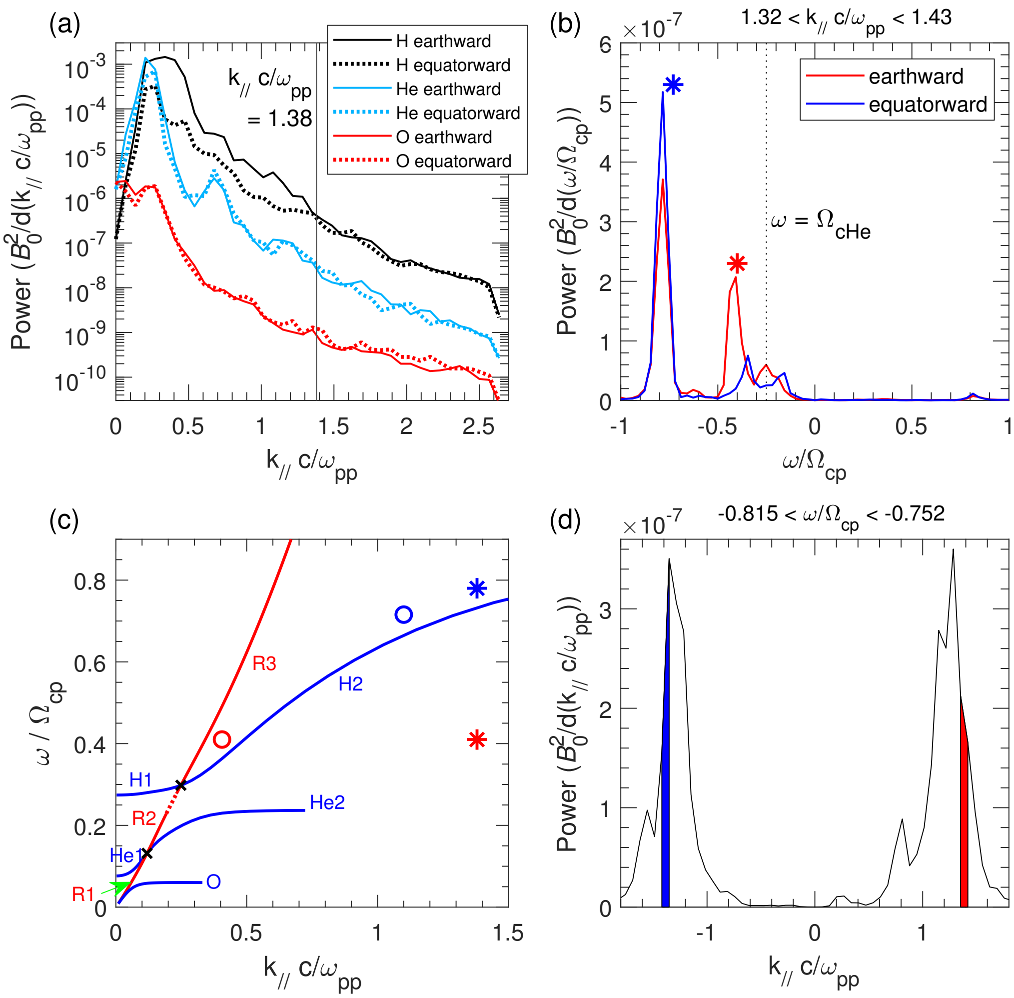

Figure 3. Wave properties at around $t = 90$ s (80–100 s) at around MLAT = 2.6° ($q = 0$–0.2). (a) Perpendicular wave magnetic field power versus $k_\parallel c/\omega_{pp}$ broken up into wavebands and portions propagating earthward or equatorward as indicated in the legend. (b) For $1.32 < k_\parallel c/\omega_{pp} < 1.43$, perpendicular wave magnetic field power versus ω/Ω_{cp} for waves propagating away from the magnetic equator (red curves) and waves propagating toward the magnetic equator (blue curves). Negative frequencies correspond to left-hand polarized waves and $|\omega/\Omega_{cp}| > 0.25$ corresponds to H band waves. (c) Dispersion surfaces for H band EMIC waves (H1 and H2), He band EMIC waves (He1 and He2), O band EMIC waves (O) and whistler waves (R1, R2, and R3) for the parameters used to generate the simulation wave data (as described by *Denton* [2018]), and positions in $k_\parallel$-ω space (asterisks) of the peaks labeled with asterisks of the same color in Figure 3a. (Figure 3c is adapted from Figure 1f of *Denton* [2018].) (d) For $-0.815 < \omega/\Omega_{cp} < -0.752$, wave power versus $k_\parallel c/\omega_{pp}$. Positive $k_\parallel$ is for waves propagating earthward.

originally generated at higher latitude (where the cyclotron frequency would be higher, and therefore the normalized wave frequency would be lower). We will be examining this possibility further below. The peak at $\omega/\Omega_{\rm cp} = -0.4$ (labeled with the red asterisk in Figure 3b) is definitely mostly propagating earthward (red curve much higher than the blue curve).

The position of the strongest peak at $\omega/\Omega_{\rm cp} = -0.8$ in $k_\parallel$-ω space is shown as the blue asterisk in Figure 3c along with the linear warm plasma dispersion curves. These curves are described in detail by *Denton* [2018] (see their Figure 1f); but here, it will suffice to note the H band labeled H2 and the He band labeled He2. Beyond $k_\parallel c/\omega_{pp} = 0.72$, where the He2 surface ends, the He band is damped. The blue asterisk in Figure 3c is close to, but not exactly on, the H band dispersion surface (H2). The broader peak at $\omega/\Omega_{\rm cp} = -0.4$ (labeled with a red asterisk in Figure 3b) is not close to a linear dispersion surface, as shown by the position of the red asterisk in Figure 3c relative to the dispersion curves. This suggests that the peak at lower frequency could be a harmonic of the dominant waves [e.g., *Usanova et al.*, 2018] or generated by some other kind of nonlinear wave–wave interaction. Note that harmonic-like peaks appear versus frequency in Figure 4 of *Denton* [2018] and versus $k_\parallel$ in Figure 5 of *Denton* [2018].

As mentioned above, within the peak at $\omega/\Omega_{\rm cp} = -0.8$ in Figure 3b, the wave power is propagating somewhat more equatorward than earthward. To see if this tendency occurs generally around $\omega/\Omega_{\rm cp} = -0.8$, we use the frequency range of that peak, $-0.815 < \omega/\Omega_{\rm cp} < -0.752$, to plot the $k_\parallel$ distribution of the wave power (not limited to $1.32 < k_\parallel c/\omega_{\rm pp} < 1.43$) in Figure 3d. Here and elsewhere positive $k_\parallel$ corresponds to earthward propagation (away from the magnetic equator). The portions of the curves with the blue and red shading are limited to the $1.32 < k_\parallel c/\omega_{\rm pp} < 1.43$ range used for Figure 3b, and show that the equatorward wave power is stronger than the earthward wave power in that range, consistent with the blue curve being higher than the red curve in Figure 3b. But away from this narrow range, the wave power appears to be about equal propagating earthward (positive $k_\parallel$ in Figure 3d) or equatorward (negative $k_\parallel$ in Figure 3d).

So it is not clear from Figure 3d that the wave power in the $\omega/\Omega_{\rm cp} = -0.8$ peak of Figure 3b is mostly propagating equatorward. But the MLAT = 2.6° location used for the data shown in Figure 3 is very close to the magnetic equator, so there is little difference between the distance from high MLAT locations in the northern and southern hemisphere.

Figures 4a and 4b are like Figures 3a and 3d, except that these are found at an earlier time around $t = 70$ s (60–80 s) at around MLAT = 7.9° (q = 0.2– 0.4). We chose the earlier time so that the waves at higher latitude might have propagated to MLAT = 2.6° by $t = 90$ s. At high $k_{\|}$, the H band waves are again dominant (black curves higher than cyan and red curves in Figure 4a), though at this time and location, by far the strongest waves are in the He band at lower $k_{\|}$.

Figure 4b shows that at $t = 70$ s at MLAT = 7.9°, the wave power for $-0.815 < \omega/\Omega_{\rm cp} < -0.752$ is dominantly equatorward. Note that the wave frequency is conserved as waves propagate; and since $\Omega_{\rm cp}$ is the value at the magnetic equator (rather than locally varying), the frequency range used for Figure 4b is the same as was used for Figure 3d. Note also from Figure 4b that the wave power at this frequency is at a lower value of $k_{\|}c/\omega_{pp} \sim 1.1$. Figure 3c plots as the blue circle this $k_{\|}$ value along with a reduced value of ω found by normalizing to the local value of the proton gyrofrequency at MLAT = 7.9°. (With fixed frequency, the local value of the cyclotron frequency, $\Omega_{\rm cp,loc}$, increases as B, and hence $\omega/\Omega_{\rm cp,loc}$ decreases away from the magnetic equator.) The fact that the blue asterisk and the blue circle lie roughly along the H2 dispersion curve shows that the waves at MLAT = 7.9° could have propagated to MLAT = 2.6°. Note also that the H band wave power is dominantly propagating equatorward for a large range of of $k_{\|}c/\omega_{pp}$ at and above 1.05, as shown by the dotted black curve being higher than the solid black curve in Figure 4a.

This suggests then, that at least some of the wave power at $-0.815 < \omega/\Omega_{\rm cp} < -0.752$ is propagating equatorward from even higher latitude. That does not, however, totally solve the problem of where these waves came from, because even at higher latitudes it will be difficult to explain the generation of waves with this frequency. Figure 5 shows wavelet analysis of the azimuthal component of the magnetic field, B_s, along the $r = 0.998$ dipole field line (almost the central field line of the simulation) at five different values of MLAT indicated in the white panel labels. While there is some wave power at $0.752 < |\omega/\Omega_{\rm cp}| < 0.815$, clearly coherent structures seem to be limited to lower frequencies.

A similar analysis to that of Figure 4 for the peak at $\omega/\Omega_{\rm cp} = -0.4$ finds that the wave power is predominantly propagating earthward, even at higher latitude. So that wave power is probably locally generated and related to the mostly earthward propagating wave

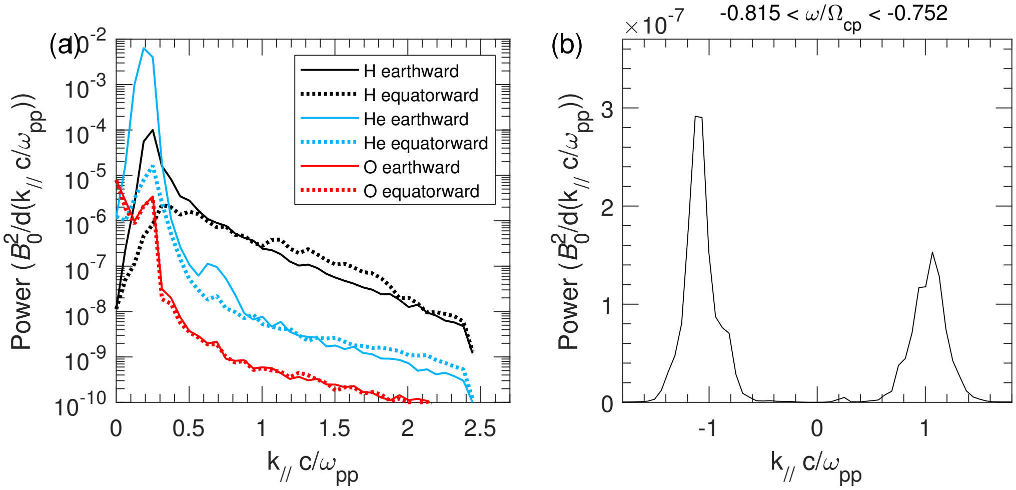

Figure 4. Wave properties at around $t = 70$ s at around MLAT = 7.9°. Figures 4a and 4b are like Figures 3a and 3d, except at the earlier time and larger MLAT.

power at lower $k_\parallel c/\omega_{pp}$ (solid black curve above dotted black curve in Figure 3a for $k_\parallel c/\omega_{pp} < 1.3$). Figure 6 is like Figure 3d, except that the frequency range is now that of the lower frequency earthward propagating (red curve) peak in Figure 3b at $-0.455 < \omega/\Omega_{\rm cp} < -0.376$. As in Figure 3d, the red and blue shadings indicate the range of $k_\parallel$ that could be in resonance with the 0.55 MeV electron. The larger wave power for earthward propagation (red shading, marked by the red asterisk in Figure 6) appears to be at the high-end of a harmonic peak. While, as noted before, the $k_\parallel$ value of this peak is not consistent with the linear dispersion relation (red asterisk far from the H2 dispersion curve in Figure 3c), the $k_\parallel$ "fundamental mode" at about $k_\parallel c/\omega_{pp} = 0.4$ (marked in Figure 6 by a red circle) is roughly consistent with the H2 linear dispersion surface, as shown by the red circle in Figure 3c.

The wave power at $k_\parallel c/\omega_{pp} \sim 0.4$ and $\omega/\Omega_{\rm cp} \sim 0.4$ (red circle in Figure 3c) may have resulted from a "rising tone" structure in the H band, as can be seen in Figure 5a at t = 68–84 s, and more clearly in Figure 5b from t = 73–94 s. Some increase in frequency with time can also be seen in the He band (for instance, at t = 42–62 s and at t = 62–74 s in Figure 5a).

While we cannot say that we totally understand the source of the high $k_\parallel$ waves, Figure 3b shows clearly that most of the wave power effective for scattering the 0.55 MeV electron was in the H band. At t = 90 s, the wave power at MLAT = 2.6° is mostly in the

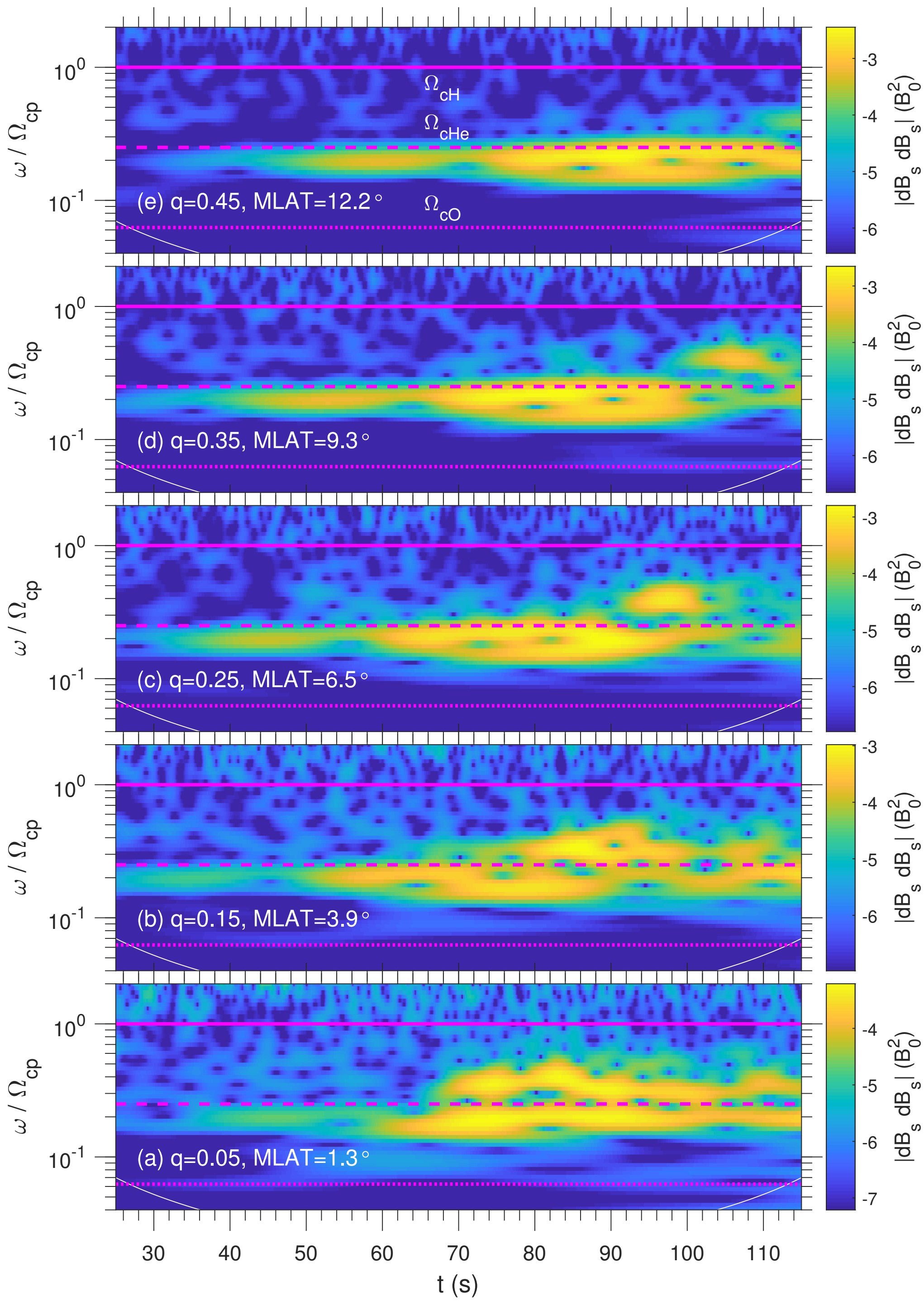

Figure 5. Wavelet analysis for the azimuthal component of the magnetic field, B_s, at $r = 0.998$ and at five different values of q and MLAT, as indicated by the panel labels. The color indicates the wave power (squared amplitude) versus time on the horizontal axis and frequency on the vertical axis. The dotted, dashed, and solid horizontal magenta lines are plotted respectively at the O+, He+, and H+ gyrofrequencies as determined at the magnetic equator. The white curve at the bottom corners of the plot shows the "cone of influence"; below this curve edge effects contaminate the results.

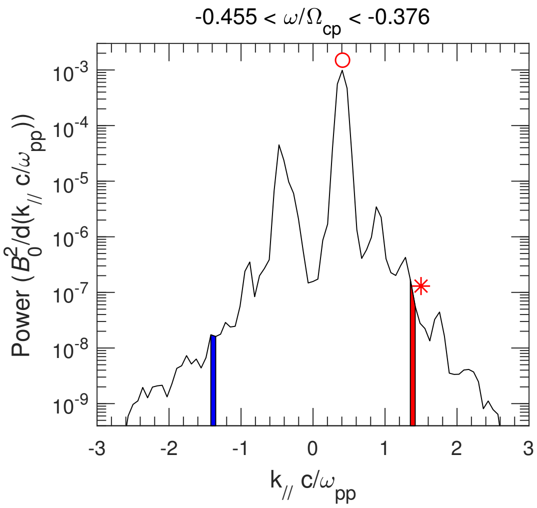

Figure 6. Wave power versus $k_{\|}c/\omega_{pp}$ at $t = 90$ s (80–100 s) at around MLAT = 2.6° ($q = 0$–0.2) like in Figure 3d, except for a different range of frequency, $-0.455 < \omega/\Omega_{cp} < -0.376$. Positive $k_{\|}$ is for waves propagating earthward.

H band (Figure 3a), though at earlier times (Figure 5a) and at higher MLAT (Figures 4a and 5c–e), the largest wave power is in the He band. Overall, the largest wave power is in the He band (Figure 4 of *Denton* [2018]).

3 EMIC simulations in straight magnetic field geometry

Now we examine the k space spectra of EMIC waves in straight magnetic field geometry. Figure 7 shows the distributions of wave power versus $k_{\|}c/\omega_{pp}$ in the three EMIC wave bands, H band (solid black curves), He band (cyan curves), and O band (red curves), for EMIC simulations in straight magnetic field geometry using 29 different sets of parameters. (There are 35 panels in Figure 7, but the five panels with green labels are all for the same simulation, the two panels with blue labels are for the same simulation, and the two panels with red labels are for the same simulation.)

The simulations were described by *Ofman et al.* [2017]. They employed two-dimensional hybrid code simulations in straight geometry. Seven sweeps in which one parameter was varied were examined (see their Table 1). In Figure 7, each row of panels shows the results from one of those sweeps. The base set of parameters for the runs can be found in the green labels of panels Ac, Bc, Cc, Dc, and Ec in Figure 7. That is, the base run had hot proton parallel plasma beta of 0.4 with anisotropy $A_h \equiv T_{\perp,\mathrm{h}}/T_{\|,\mathrm{h}} = 1$, and concentra-

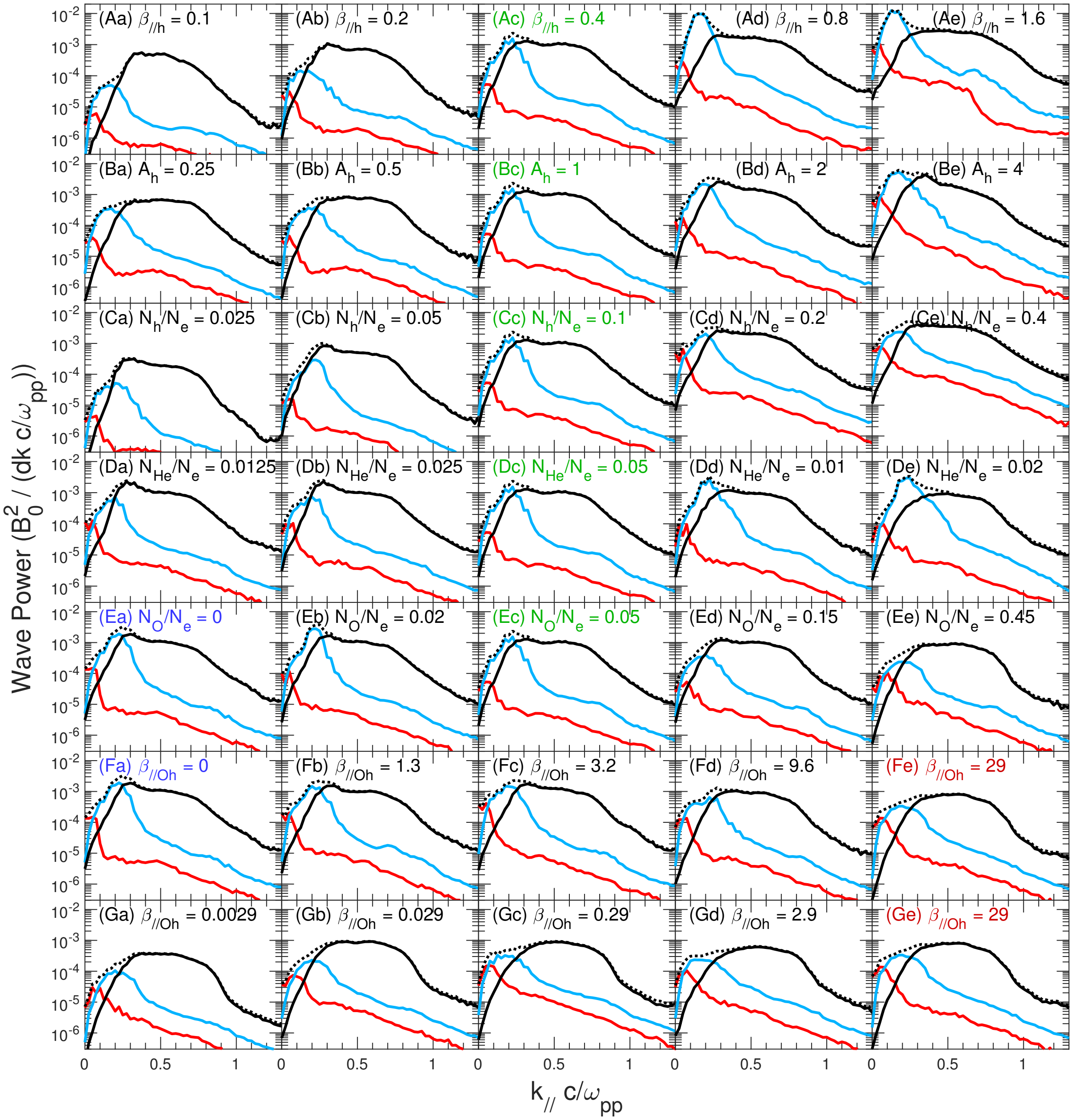

Figure 7. Total wave power (dotted black curves), and wave power in the H band (solid black curves), He band (cyan curves), and O band (red curves) versus $k_{\parallel}$ for hybrid code EMIC simulations in straight geometry for a variety of parameters. In each horizontal row, the parameter listed in the panel label is varied. The simulations with black panel labels are unique, but the simulations with green, blue, or red panel labels are the same as the others with the same colored label. For instance, the curves in panel Ac (with the green label) are the same as those in panels Bc, Cc, Dc, and Ec.

tions of density relative to the electron density of 0.1, 0.05, and 0.05 for hot protons, cold He+, and cold O+. Given these concentrations of ions, the concentration of cold H+ is the remaining amount necessary to achieve quasi-neutrality.

While sweeps 1–5 of *Ofman et al.* [2017] varied just one parameter around these base parameters, sweeps 6 and 7 were slightly different. In sweep 6, the O+ was all hot with a temperature of 160 keV. This temperature was chosen to make the thermal velocity of the O+ comparable to the Alfvén speed. In sweep 7, the temperature of the O+ was varied using a large O+ concentration of 0.45. Given this information, the parameters for each simulation can be obtained from the value of the parameter listed in each label of Figure 7. For instance, Figure 7Aa uses all the base parameters, $A_\mathrm{h} = 1$, $N_\mathrm{h}/N_\mathrm{e} = 0.1$, $N_\mathrm{He}/N_\mathrm{e} = 0.05$, and $N_\mathrm{O}/N_\mathrm{e} = 0.05$, except for the one parameter listed in the label of Figure 7Aa, $\beta_{\|,\mathrm{h}} = 0.1$, which was varied by changing the temperature of the hot protons. For the precise parameters used for the simulations, see Table 1 of *Ofman et al.* [2017] and their description.

Though we can see the specific parameters in the runs used for Figure 7, our purpose for showing this figure is to identify something that is the same for every one of these runs. For $k_\| c/\omega_\mathrm{pp}$ greater than a value between 0.3 and 0.4, the H band (solid black curves) has the greatest wave power. For most of these runs the H band waves had the highest amplitude. But for the runs with wave power distributions shown in Figure 7Ae and 7De, the He band has the highest amplitude waves. There is no significant difference in the distribution of wave power for high $k_\| c/\omega_\mathrm{pp}$, however, for any of the runs. At those values of $k_\| c/\omega_\mathrm{pp}$, the wave power in the H band is always dominant.

4 Discussion

While there have been good reasons to believe that EMIC waves can strongly affect ultra-relativistic electrons with energies above 2 MeV [*Meredith et al.*, 2003; *Shprits et al.*, 2016], it has been less clear how EMIC waves could affect sub-MeV relativistic electrons. Yet recent observational results have suggested that precipitating electrons may have such low energies [*Millan et al.*, 2007; *Zhang et al.*, 2016; *Hendry et al.*, 2017, and references therein]. The *Hendry et al.* [2017] results, using a very large database of precipitation events observed by the POES spacecraft [see also *Carson et al.*, 2013; *Hendry et al.*, 2016], are particularly important. Only events were included for which there was simultaneous proton precipitation, suggesting EMIC waves as a likely cause because EMIC waves also scatter ring current protons. *Hendry et al.* [2016] showed that the probability was very high, as high as 90%, for EMIC waves to be observed by ground magnetometers at locations mapped to that of the POES. Other case studies have also demonstrated a connection between precipitation events and EMIC waves [*Clilverd et al.*, 2013; *Blum et al.*, 2015; *Clilverd et al.*, 2015; *Rodger et al.*, 2015; *Hendry et al.*, 2016, 2017]. It is possible that other mechanisms might be responsible for some of the *Hendry et al.* [2017] events [see, e.g. *Yahnin et al.*, 2016; *Smith et al.*, 2016; *Shekhar et al.*, 2018]. But it seems that many of these events probably are caused by EMIC waves. Results by *Rodger et al.* [2018] suggest that precipitating electrons may be dominantly low-energy, even if the equatorial distribution of those particles is relatively unaffected, simply because there are so many more of them. Even though ultra-relativistic electrons may be most affected, no precipitation has been observed at those energies. Indeed, it is not clear that any current observations could detect precipitation of such high-energy particles.

But the question of how EMIC waves can affect sub-MeV relativistic electrons remains to be explained. Using test particles in the wave fields of a hybrid code simulation in dipole geometry, we have shown that there can be significant diffusion and precipitation of sub-MeV relativistic electrons (Figure 1). The required pitch angle scattering can occur through interaction of the particles with low amplitude EMIC wave power with relatively high $k_\parallel c/\omega_{\rm pp}$ (section 2.4). As shown by *Denton* [2018] [see also *Ukhorskiy et al.*, 2010], EMIC waves can have a broad distribution with a high $k_\parallel$ tail (see, e.g., Figure 5A of *Denton* [2018]). We have shown that it is the high $k_\parallel c/\omega_{\rm pp}$ part of the wave power spectrum that leads to significant pitch angle scattering of a 0.55 MeV electron (Figure 2).

A mechanism for nonresonant interactions of sub-MeV electrons with EMIC waves has recently been proposed [*Chen et al.*, 2016]. But our examination of a particular particle suggests that resonant scattering with low amplitude waves is responsible for the pitch angle scattering (section 2.4).

The wave power that scattered the 0.55 MeV particle discussed in section 2.4 was in the EMIC H band, rather than the He band. At least some of the wave power that scattered the 0.55 MeV electron appears to have propagated down the H band dispersion surface from higher latitude (based on Figure 4b), suggesting that the geometry of the dipole magnetic field might have played an important role in the production of these waves.

Some of the wave power seems to have arisen through harmonics of a rising tone H band wave (Figures 6 and 5).

Simulations in straight magnetic field geometry suggest that the high $k_{\|}c/\omega_{\rm pp}$ part of the spectrum may always be in the H band. The H band spectrum has a fairly similar shape for all of the simulations shown in Figure 7. To model the effect of EMIC waves on a broad range of particle energies, it would be useful to model this part of the spectrum.

In summary, we have shown how EMIC waves can pitch angle scatter sub-MeV relativistic electrons with energy well below the resonant energy of the highest amplitude waves. At these energies, the pitch angle scattering is more effective at small pitch angles than at large ones (Figures 1c and 1f). Relativistic electron distributions for which the pitch angle distribution of relativistic electrons is narrowed closer to 90° pitch angle, but otherwise relatively unaffected [*Usanova et al.*, 2014], might be in this sub-resonance energy range. Strong scattering occurs when the energy is above the minimum resonant energy (Figures 1f). Our results suggest that the wave power that scatters sub-MeV relativistic electrons is normally in the EMIC H band, even when the highest amplitude waves are in the He band.

He band EMIC waves have received more attention than H band EMIC waves in analysis of relativistic electron loss. Relativistic electron precipitation events are more likely to occur on the dusk side of the Earth [*Millan and Thorne*, 2007; *Comess et al.*, 2013; *Shekhar et al.*, 2017]; and He band EMIC waves are also more likely to occur on the dusk side [*Min et al.*, 2012; *Saikin et al.*, 2015; *Halford et al.*, 2016] (see also discussion by *Qin et al.* [2018]). H band wave occurrence has peaks in the morning and afternoon local time sectors [*Saikin et al.*, 2015; *Tetrick et al.*, 2017]. *Hendry et al.* [2017] recently found that relativistic precipitation events correlated with He band events with rising frequency. And there is support for the idea that waves with increasing frequency can be effective for pitch angle scattering [*Kubota and Omura*, 2017, and references therein].

But a recent study using Van Allen Probes data to identify EMIC waves, and then examining the probability of relativistic electron precipitation measured by the POES satellites, found some surprising results. *Qin et al.* [2018] found that the proportion of H band EMIC wave events that were associated with relativistic electron precipitation (22% to 32%) was slightly higher than for He band EMIC wave activity (18% to 27%). An even greater proportion (25% to 40%) of EMIC waves was accompanied by relativistic electron precipitation events when H band and He band EMIC waves occurred simultaneously. The only study we are aware of that looked at the local time dependence of simultaneous occurrence of He and H band waves is that of *Tetrick et al.* [2017]. They found peak distribution in the afternoon local time sector, with the next highest probability in the pre-midnight local time sector. One point of confusion is that these events were preferentially inside the plasmapause, whereas the *Hendry et al.* [2017] events with rising frequency seemed to be preferentially outside the plasmapause.

Our results make clear the importance of the H band waves. But why then would the He band waves be important? Possibly the presence of He band waves is an indicator of another underlying cause. The He band waves are more likely to occur in regions with high density [*Denton et al.*, 2014]. The plasma density is higher on the dusk side where there may be a plasmaspheric bulge or plume-like structure, and where even the plasmatrough density is enhanced [*Denton et al.*, 2006]. As discussed in the Introduction, larger density leads to larger $k_{\|}$, which leads to a smaller minimum resonant energy.

While both EMIC waves and precipitation events are more likely to occur on the dusk side of the earth, there is a significant difference in the distribution [as discussed by, e.g., *Smith et al.*, 2016]. While the peak occurrence of EMIC waves (especially for He band waves) seems to be in the afternoon sector (MLT = 12–18) [*Anderson et al.*, 1992; *Min et al.*, 2012; *Saikin et al.*, 2015; *Halford et al.*, 2016], the distribution of relativistic electron precipitation events seems to be shifted into the pre-midnight sector (MLT = 18–24) [*Comess et al.*, 2013; *Carson et al.*, 2013; *Woodger et al.*, 2018]. The *Carson et al.* [2013] database with simultaneous proton precipitation (on which the *Hendry et al.* [2016, 2017] results were based) finds the distribution of events extending past midnight to about MLT = 2, and the occurrence at MLT = 12 is very low compared to the occurrence of EMIC waves. As mentioned above, it is possible that at least some of the events resulted from another mechanism such as curvature scattering, which will occur most strongly at midnight local time [*Yahnin et al.*, 2016; *Smith et al.*, 2016; *Shekhar et al.*, 2018], though we feel that more work needs to be done to validate that as a cause of the relativistic electron precipitation.

Usanova et al. [2013] pointed out that the region of greatest occurrence of plasmaspheric plumes was shifted toward midnight relative to peak occurrence of EMIC waves, supporting the connection to density mentioned above. The probability of EMIC waves is greater when the density is enhanced [*Halford et al.*, 2015], though EMIC events are not necessarily located in plasmaspheric plumes [*Halford et al.*, 2015; *Tetrick et al.*, 2017]. *Woodger et al.* [2018] show that the most energetic EMIC events occur in regions of larger magnetic field, which would favor the dayside where the magnetic field is compressed. Thus the more common lower energy events that are more easily observed (because lower energy particles are more prevalent and because there are no ultra-relativistic electron precipitation detectors) may occur closer to midnight. The ring current proton density peaks near midnight, and the ring current proton parallel temperature peaks in the pre-midnight local time sector [*Denton et al.*, 2005]. (The ring current proton perpendicular temperature peaks in the afternoon local time sector.) Thus the ring current plasma pressure and plasma beta will be high in the pre-midnight local time sector.

But we do not currently understand why these plasma conditions would be most favorable for sub-MeV electron precipitation. Results by *Denton et al.* [2015] would suggest that higher parallel temperature would correlate with higher energy relativistic electron precipitation. As noted previously, *Hendry et al.* [2016] found a correlation between precipitation events and rising tone He band EMIC; they also found that the distribution of this kind of event was shifted into the pre-midnight local time sector. At this point, the distribution of the precipitation events is not totally understood.

While both the uniform magnetic field geometry simulations (section 3) and the simulation in a dipole magnetic field (section 2) indicate that the high $k_{\|}$ portion of the EMIC waves spectrum is predominantly in the H band, there are some significant differences in the detailed spectrum. Figure 3 suggests that at least some of the wave power scattering the 0.55 MeV electron came from higher latitude. Figure 5 shows evidence of rising tone structures that may lead to higher $k_{\|}$ in the H band. While the simulation fields that we have used [*Denton*, 2018] are far more realistic than what has previously been used for test particle simulations, the wave fields in the magnetosphere may be even more complex. For instance, *Denton* [2018] started his simulation from a quiet equilibrium and used a large number of particles to lower the noise. Waves in the real magnetosphere may be far more noisy. Future investigations should focus on observations of the detailed spatial structure of waves, including the high $k_{\|}$ spectrum of EMIC waves. These studies should also include very low frequency (VLF) and ultra low frequency (ULF) waves, and modeling how particles interact with these waves.

Acknowledgments

RED was supported by NSF grant AGS-1602469 and NASA grant 80NSSC19K0270. LO acknowledges support by NASA Cooperative Agreement NNG11PL10A to The Catholic University of America. The wave fields used for this study are available in a Zenodo data repository at https://doi.org/10.5281/zenodo.1009668. The particle position, velocity, and fields at the particle position that were used to make Figure 2 are in the supplementary data file, DentonEmicPas19_ds01.csv. We thank Jay Albert for useful conversations.

References

Albert, J. M., and J. Bortnik (2009), Nonlinear interaction of radiation belt electrons with electromagnetic ion cyclotron waves, *Geophys. Res. Lett.*, p. L12110 (5 pp.), doi: 10.1029/2009gl03 8904.

Anderson, B. J., R. E. Erlandson, and L. J. Zanetti (1992), A statistical study of PC 1-2 magnetic pulsations in the equatorial magnetosphere. 1. Equatorial occurrence distributions, *J. Geophys. Res.*, *97*(A3), 3075–3088, doi:10.1029/91ja02706.

Andre, M. (1985), Dispersion surfaces, *Journal of Plasma Physics*, *33*(FEB), 1–19.

Aseev, N. A., Y. Y. Shprits, A. Y. Drozdov, A. C. Kellerman, M. E. Usanova, D. Wang, and I. S. Zhelavskaya (2017), Signatures of ultrarelativistic electron loss in the heart of the outer radiation belt measured by Van Allen Probes, *J. Geophys. Res.*, *122*(10), 10,102–10,111, doi:10.1002/2017ja024485.

Blum, L. W., A. Halford, R. Millan, J. W. Bonnell, J. Goldstein, M. Usanova, M. Engebretson, M. Ohnsted, G. Reeves, H. Singer, M. Clilverd, and X. Li (2015), Observations of coincident EMIC wave activity and duskside energetic electron precipitation on 18-19 January 2013, *Geophys. Res. Lett.*, *42*(14), 5727–5735, doi:10.1002/2015gl065245.

Carson, B. R., C. J. Rodger, and M. A. Clilverd (2013), POES satellite observations of EMIC-wave driven relativistic electron precipitation during 1998-2010, *J. Geophys. Res.*, *118*(1), 232–243, doi:10.1029/2012ja017998.

Chen, L. J., R. M. Thorne, J. Bortnik, and X. J. Zhang (2016), Nonresonant interactions of electromagnetic ion cyclotron waves with relativistic electrons, *J. Geophys. Res.*, *121*(10), 9913–9925, doi:10.1002/2016ja022813.

Clilverd, M. A., N. Cobbett, C. J. Rodger, J. B. Brundell, M. H. Denton, D. P. Hartley, J. V. Rodriguez, D. Danskin, T. Raita, and E. L. Spanswick (2013), Energetic electron precipitation characteristics observed from Antarctica during a flux dropout event, *J.*

Geophys. Res., *118*(11), 6921–6935, doi:10.1002/2013ja019067.

Clilverd, M. A., R. Duthie, R. Hardman, A. T. Hendry, C. J. Rodger, T. Raita, M. Engebretson, M. R. Lessard, D. Danskin, and D. K. Milling (2015), Electron precipitation from EMIC waves: A case study from 31 May 2013, *J. Geophys. Res.*, *120*(5), 3618–3631, doi:10.1002/2015ja021090.

Comess, M. D., D. M. Smith, R. S. Selesnick, R. M. Millan, and J. G. Sample (2013), Duskside relativistic electron precipitation as measured by SAMPEX: A statistical survey, *J. Geophys. Res.*, *118*(8), 5050–5058, doi:10.1002/jgra.50481.

Cornwall, J. M. (1965), Cyclotron instabilities and electromagnetic emission in ultra low frequency and very low frequency ranges, *Journal of Geophysical Research*, *70*(1), 61, doi:10.1029/JZ070i001p00061.

Denton, M. H., M. F. Thomsen, H. Korth, S. Lynch, J. C. Zhang, and M. W. Liemohn (2005), Bulk plasma properties at geosynchronous orbit, *J. Geophys. Res.*, *110*(A7), doi:10.1029/2004ja010861.

Denton, R. E. (2018), Electromagnetic ion cyclotron wavefields in a realistic dipole field, *J. Geophys. Res.*, *123*(2), 1208–1223, doi:10.1002/2017ja024886.

Denton, R. E., J. Goldsten, D. H. Lee, R. A. King, Z. C. Dent, D. L. Gallagher, D. Berube, K. Takahashi, M. Nose, D. Milling, and F. Honary (2006), Realistic magnetospheric density model for 29 august 2000, *J. Atmos. Sol.-Terr. Phys.*, *68*(6), 615–628, doi:10.1016/j.jastp.2005.11.009.

Denton, R. E., V. K. Jordanova, and B. J. Fraser (2014), Effect of spatial density variation and O+ concentration on the growth and evolution of electromagnetic ion cyclotron waves, *J. Geophys. Res.*, *119*(10), 8372–8395, doi:10.1002/2014ja020384.

Denton, R. E., V. K. Jordanova, and J. Bortnik (2015), Resonance of relativistic electrons with electromagnetic ion cyclotron waves, *Geophys. Res. Lett.*, *42*(20), 8263–8270, doi:10.1002/2015gl064379.

Halford, A. J., B. J. Fraser, and S. K. Morley (2015), EMIC waves and plasmaspheric and plume density: CRRES results, *J. Geophys. Res.*, *120*, 1974âĂŞ1992, doi:10.1002/2014JA020338.

Halford, A. J., B. J. Fraser, S. K. Morley, S. R. Elkington, and A. A. Chan (2016), Dependence of EMIC wave parameters during quiet, geomagnetic storm, and geomagnetic storm phase times, *J. Geophys. Res.*, *121*(7), 6277–6291, doi:10.1002/2016ja022694.

Hendry, A. T., C. J. Rodger, M. A. Clilverd, M. J. Engebretson, I. R. Mann, M. R. Lessard, T. Raita, and D. K. Milling (2016), Confirmation of EMIC wave-driven relativistic electron precipitation, *J. Geophys. Res.*, *121*(6), 5366–5383, doi: 10.1002/2015ja022224.

Hendry, A. T., C. J. Rodger, and M. A. Clilverd (2017), Evidence of sub-MeV EMIC-driven electron precipitation, *Geophys. Res. Lett.*, *44*(3), 1210–1218, doi: 10.1002/2016gl071807.

Hu, Y. (2010), Hybrid code simulation of electromagnetic ion cyclotron waves in curvilinear coordinates, (Ph.D. dissertation), Hanover, NH: Dartmouth College, Ph.D. thesis.

Hu, Y., R. E. Denton, and J. R. Johnson (2010), Two-dimensional hybrid code simulation of electromagnetic ion cyclotron waves of multi-ion plasmas in a dipole magnetic field, *J. Geophys. Res.*, *115*, a09218, doi:10.1029/2009ja015158.

Hyun, K., K. H. Kim, E. Lee, H. J. Kwon, D. H. Lee, and H. Jin (2014), Loss of geosynchronous relativistic electrons by EMIC wave scattering under quiet geomagnetic conditions, *J. Geophys. Res.*, *119*(10), 8357–8371, doi:10.1002/2014ja020234.

Kennel, C. F. (1969), Consequences of a magnetispheric plasma, *Reviews of Geophysics*, *7*(1-2), 379.

Kennel, C. F., and H. E. Petschek (1966), Limit on stably trapped particle fluxes, *Journal of Geophysical Research*, *71*(1), 1.

Kersten, T., R. B. Horne, S. A. Glauert, N. P. Meredith, B. J. Fraser, and R. S. Grew (2014), Electron losses from the radiation belts caused by EMIC waves, *J. Geophys. Res.*, *119*(11), 8820–8837, doi:10.1002/2014ja020366.

Kubota, Y., and Y. Omura (2017), Rapid precipitation of radiation belt electrons induced by EMIC rising tone emissions localized in longitude inside and outside the plasmapause, *J. Geophys. Res.*, *122*(1), 293–309, doi:10.1002/2016ja023267.

Li, W., Y. Y. Shprits, and R. M. Thorne (2007), Dynamic evolution of energetic outer zone electrons due to wave-particle interactions during storms, *J. Geophys. Res.*, *112*(A10), a10220, doi:10.1029/2007ja012368.

Li, Z., R. M. Millan, M. K. Hudson, L. A. Woodger, D. M. Smith, Y. Chen, R. Friedel, J. V. Rodriguez, M. J. Engebretson, J. Goldstein, J. F. Fennell, and H. E. Spence (2014), Investigation of EMIC wave scattering as the cause for the BARREL 17 January 2013 relativistic electron precipitation event: A quantitative comparison of simulation with observations, *Geophys. Res. Lett.*, *41*(24), 8722–8729, doi:10.1002/2014gl062273.

Meredith, N. P., R. M. Thorne, R. B. Horne, D. Summers, B. J. Fraser, and R. R. Anderson (2003), Statistical analysis of relativistic electron energies for cyclotron resonance with EMIC waves observed on CRRES, *J. Geophys. Res.*, *108*(A6), 1250, doi: 10.1029/2002ja009700.

Millan, R. M., and R. M. Thorne (2007), Review of radiation belt relativistic electron losses, *J. Atmos. Sol.-Terr. Phys.*, *69*(3), 362–377, doi:10.1016/j.jastp.2006.06.019.

Millan, R. M., R. P. Lin, D. M. Smith, and M. P. McCarthy (2007), Observation of relativistic electron precipitation during a rapid decrease of trapped relativistic electron flux, *Geophys. Res. Lett.*, *34*(10), doi:10.1029/2006gl028653.

Min, K., J. Lee, K. Keika, and W. Li (2012), Global distribution of EMIC waves derived from THEMIS observations, *J. Geophys. Res.*, *117*, a05219, doi:10.1029/2012ja017515.

Miyoshi, Y., K. Sakaguchi, K. Shiokawa, D. Evans, J. Albert, M. Connors, and V. Jordanova (2008), Precipitation of radiation belt electrons by EMIC waves, observed from ground and space, *Geophys. Res. Lett.*, p. L23101 (5 pp.), doi:10.1029/2008gl035727.

Ofman, L., R. E. Denton, J. Bortnik, X. An, A. Glocer, and C. Komar (2017), Growth and nonlinear saturation of electromagnetic ion cyclotron waves in multi-ion species magnetospheric plasma, *J. Geophys. Res.*, *122*(6), 6469–6484, doi:10.1002/2017ja024172.

Qin, M. R., M. Hudson, R. Millan, L. Woodger, and S. Shekhar (2018), Statistical investigation of the efficiency of EMIC waves in precipitating relativistic electrons, *J. Geophys. Res.*, *123*(8), 6223–6230, doi:10.1029/2018ja025419.

Rodger, C. J., A. T. Hendry, M. A. Clilverd, C. A. Kletzing, J. B. Brundell, and G. D. Reeves (2015), High-resolution in situ observations of electron precipitation-causing EMIC waves, *Geophys. Res. Lett.*, *42*(22), 9633–9641, doi:10.1002/2015gl066581.

Rodger, C. J., A. T. Hendry, and M. A. Clilverd (2018), Outstanding questions around the energy of EMIC wave driven electron precipitation, *AGU Chapman Conference on Particle Dynamics in the Earth's Radiation Belts, March 4–9, 2018, Caiscais, Portugal*.

Saikin, A. A., J. C. Zhang, R. C. Allen, C. W. Smith, L. M. Kistler, H. E. Spence, R. B. Torbert, C. A. Kletzing, and V. K. Jordanova (2015), The occurrence and wave properties of H+-, He+-, and O+-band EMIC waves observed by the Van Allen Probes, *J. Geophys. Res.*, *120*(9), 7477–7492, doi:10.1002/2015ja021358.

Shekhar, S., R. Millan, and D. Smith (2017), A statistical study of the spatial extent of relativistic electron precipitation with Polar Orbiting Environmental Satellites, *J. Geophys. Res.*, *122*(11), 11,274–11,284, doi:10.1002/2017ja024716.

Shekhar, S., R. M. Millan, and M. K. Hudson (2018), A statistical study of spatial variation of relativistic electron precipitation energy spectra with Polar Operational Environmental Satellites, *J. Geophys. Res.*, *123*(5), 3349–3359, doi:10.1002/2017ja025041.

Shprits, Y. Y., D. A. Subbotin, N. P. Meredith, and S. R. Elkington (2008), Review of modeling of losses and sources of relativistic electrons in the outer radiation belt. ii: Local acceleration and loss, *J. Atmos. Sol.-Terr. Phys.*, *70*(14), 1694–1713, doi: 10.1016/j.jastp.2008.06.014.

Shprits, Y. Y., L. J. Chen, and R. M. Thorne (2009), Simulations of pitch angle scattering of relativistic electrons with MLT -dependent diffusion coefficients, *J. Geophys. Res.*, *114*, doi:10.1029/2008JA013695.

Shprits, Y. Y., A. Y. Drozdov, M. Spasojevic, A. C. Kellerman, M. E. Usanova, M. J. Engebretson, O. V. Agapitov, I. S. Zhelavskaya, T. J. Raita, H. E. Spence, D. N. Baker, H. Zhu, and N. A. Aseev (2016), Wave-induced loss of ultra-relativistic electrons in the Van Allen radiation belts, *Nature Communications*, *7*, 12883, doi: 10.1038/ncomms12883.

Shprits, Y. Y., A. Kellerman, N. Aseev, A. Y. Drozdov, and I. Michaelis (2017), Multi-MeV electron loss in the heart of the radiation belts, *Geophys. Res. Lett.*, *44*(3), 1204–1209, doi:10.1002/2016gl072258.

Shprits, Y. Y., R. B. Horne, A. C. Kellerman, and A. Y. Drozdov (2018), The dynamics of Van Allen belts revisited, *Nature Physics*, *14*(2), 102–103, doi:10.1038/nphys4350.

Smith, D. M., E. P. Casavant, M. D. Comess, X. Q. Liang, G. S. Bowers, R. S. Selesnick, L. B. N. Clausen, R. M. Millan, and J. G. Sample (2016), The causes of the hardest electron precipitation events seen with SAMPEX, *J. Geophys. Res.*, *121*(9), 8600–8613, doi:10.1002/2016ja022346.

Summers, D., B. Ni, and N. P. Meredith (2007a), Timescales for radiation belt electron acceleration and loss due to resonant wave-particle interactions: 1. theory, *J. Geophys. Res.*, *112*(A4), doi:10.1029/2006JA011801.

Summers, D., B. Ni, and N. P. Meredith (2007b), Timescales for radiation belt electron acceleration and loss due to resonant wave-particle interactions: 2. evaluation for vlf chorus, elf hiss, and electromagnetic ion cyclotron waves, *J. Geophys. Res.*, *112*(A4), doi:10.1029/2006JA011993.

Tetrick, S. S., M. J. Engebretson, J. L. Posch, C. N. Olson, C. W. Smith, R. E. Denton, S. A. Thaller, J. R. Wygant, G. D. Reeves, E. A. MacDonald, and J. F. Fennell (2017), Location of intense electromagnetic ion cyclotron (EMIC) wave events relative to the plasmapause: Van Allen Probes observations, *J. Geophys. Res.*, *122*(4), 4064–4088, doi: 10.1002/2016ja023392.

Ukhorskiy, A. Y., Y. Y. Shprits, B. J. Anderson, K. Takahashi, and R. M. Thorne (2010), Rapid scattering of radiation belt electrons by storm-time EMIC waves, *Geophys. Res. Lett.*, *37*, l09101, doi:10.1029/2010gl042906.

Usanova, M. E., F. Darrouzet, I. R. Mann, and J. Bortnik (2013), Statistical analysis of EMIC waves in plasmaspheric plumes from Cluster observations, *J. Geophys. Res.*, *118*(8), 4946–4951, doi:10.1002/jgra.50464.

Usanova, M. E., A. Drozdov, K. Orlova, I. R. Mann, Y. Shprits, M. T. Robertson, D. L. Turner, D. K. Milling, A. Kale, D. N. Baker, S. A. Thaller, G. D. Reeves, H. E. Spence, C. Kletzing, and J. Wygant (2014), Effect of EMIC waves on relativistic and ultrarelativistic electron populations: Ground- based and Van Allen Probes observations, *Geophys. Res. Lett.*, *41*(5), 1375–1381, doi:10.1002/2013gl059024.

Usanova, M. E., N. Ahmadi, D. M. Malaspina, R. E. Ergun, K. J. Trattner, Q. Reece, T. Leonard, S. A. Fuselier, R. B. Torbert, C. T. Russell, and J. L. Burch (2018), MMS observations of harmonic electromagnetic ion cyclotron waves, *Geophys. Res. Lett.*, *45*(17), 8764–8772, doi:10.1029/2018gl079006.

Woodger, L. A., R. M. Millan, Z. Li, and J. G. Sample (2018), Impact of background magnetic field for EMIC wave-driven electron precipitation, *J. Geophys. Res.*, *123*(10), 8518–8532, doi:10.1029/2018ja025315.

Yahnin, A. G., T. A. Yahnina, N. V. Semenova, B. B. Gvozdevsky, and A. B. Pashin (2016), Relativistic electron precipitation as seen by NOAA POES, *J. Geophys. Res.*, *121*(9), 8286–8299, doi:10.1002/2016ja022765.

Zhang, J. C., A. J. Halford, A. A. Saikin, C. L. Huang, H. E. Spence, B. A. Larsen, G. D. Reeves, R. M. Millan, C. W. Smith, R. B. Torbert, W. S. Kurth, C. A. Kletzing, J. B. Blake, J. F. Fennel, and D. N. Baker (2016), EMIC waves and associated relativistic electron precipitation on 25-26 January 2013, *J. Geophys. Res.*, *121*(11), 11,086–11,100, doi:10.1002/2016ja022918.

Figure 1.

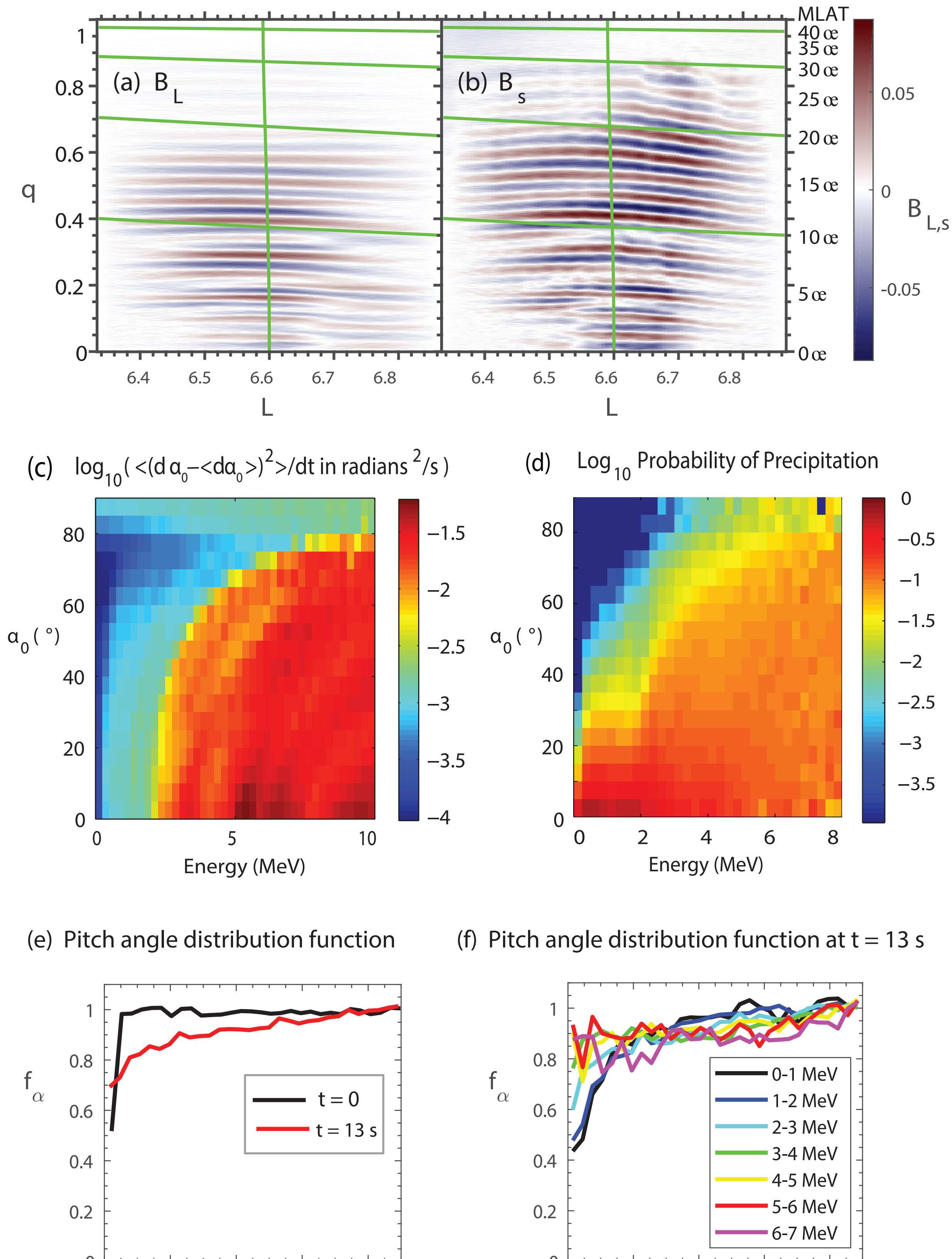

MLAT
(a) B L
(b) B s
q
L
B L,s
(c) log10(<(d α0−<dα0>)2>/dt in radians 2/s)
(d) Log 10 Probability of Precipitation
α0 (°)
Energy (MeV)
(e) Pitch angle distribution function
(f) Pitch angle distribution function at t = 13 s
fα
t = 0
t = 13 s
0-1 MeV
1-2 MeV
2-3 MeV
3-4 MeV
4-5 MeV
5-6 MeV
6-7 MeV

Figure 2.

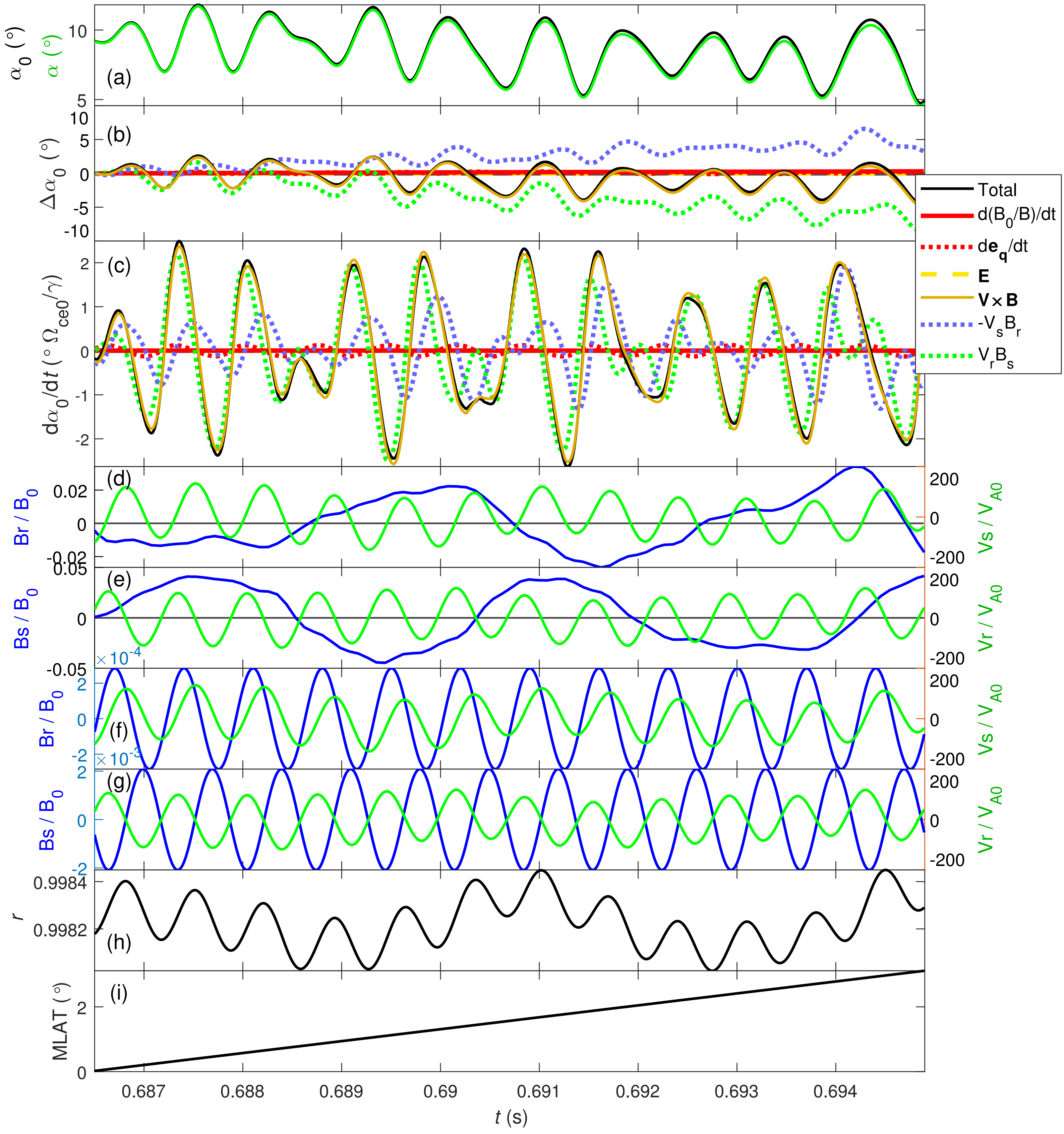

α_0 (°)
α (°)
(a)
(b)
$\Delta\alpha_0$ (°)
(c)
$d\alpha_0/dt$ (° Ω_{ce0}/γ)
Total
$d(B_0/B)/dt$
$d\mathbf{e_q}/dt$
E
$\mathbf{V\times B}$
$-V_sB_r$
V_rB_s
(d)
Br / B_0
Vs / V_{A0}
(e)
Bs / B_0
Vr / V_{A0}
(f)
Br / B_0
Vs / V_{A0}
(g)
Bs / B_0
Vr / V_{A0}
(h)
r
(i)
MLAT (°)
t (s)

Figure 3.

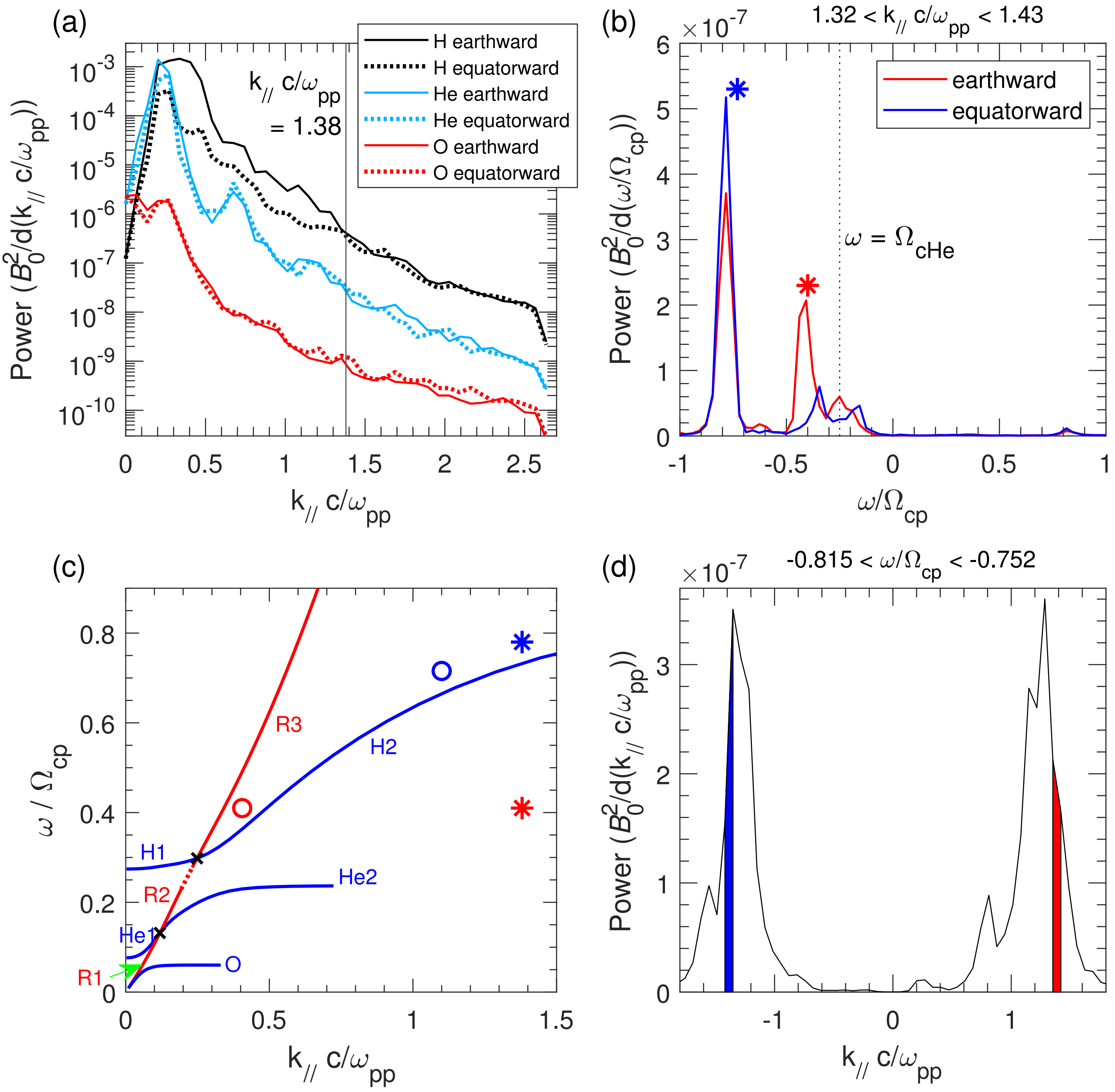

(a)
H earthward
H equatorward
He earthward
He equatorward
O earthward
O equatorward
$k_{//}\ c/\omega_{pp}$ = 1.38
Power ($B_0^2/d(k_{//}\ c/\omega_{pp})$)
$k_{//}\ c/\omega_{pp}$
(b)
$\times 10^{-7}$
$1.32 < k_{//}\ c/\omega_{pp} < 1.43$
earthward
equatorward
$\omega = \Omega_{cHe}$
Power ($B_0^2/d(\omega/\Omega_{cp})$)
ω/Ω_{cp}
(c)
R3
H2
H1
He2
R2
He1
O
R1
$\omega\ /\ \Omega_{cp}$
$k_{//}\ c/\omega_{pp}$
(d)
$\times 10^{-7}$
$-0.815 < \omega/\Omega_{cp} < -0.752$
Power ($B_0^2/d(k_{//}\ c/\omega_{pp})$)
$k_{//}\ c/\omega_{pp}$

Figure 4.

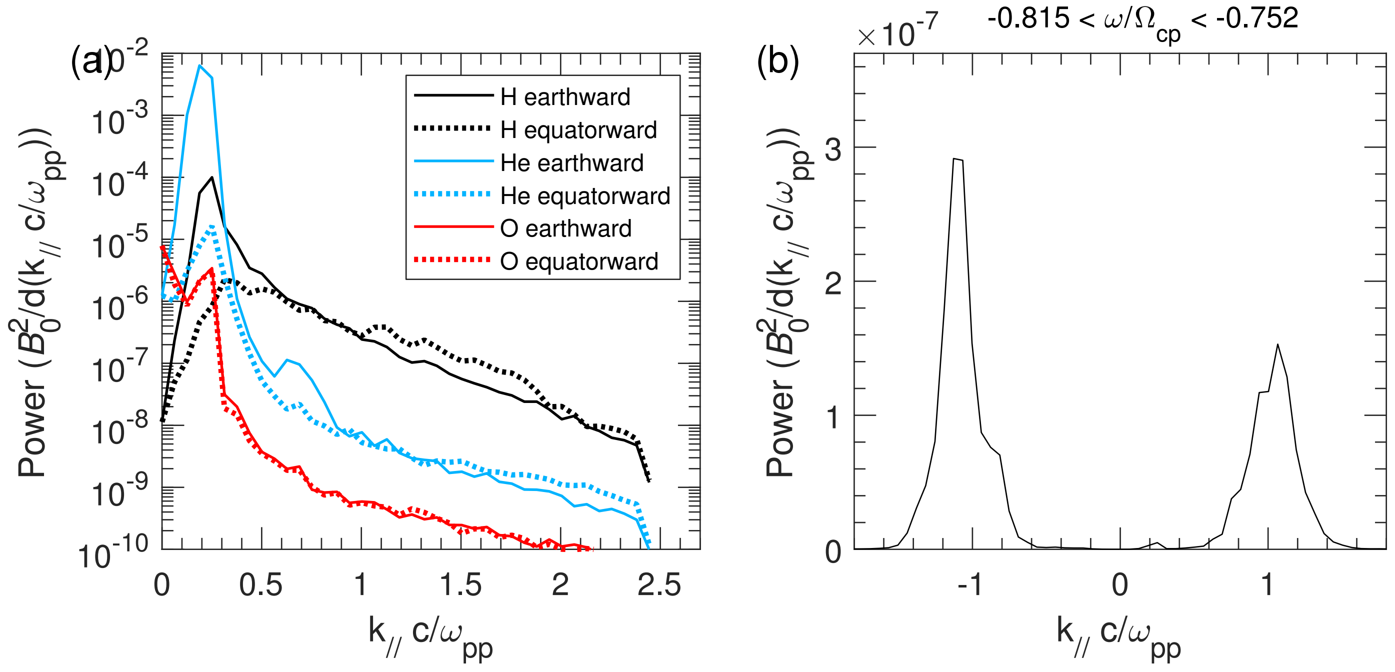

(a)
H earthward
H equatorward
He earthward
He equatorward
O earthward
O equatorward
Power (B_0^2/d($k_{//}$ c/ω_{pp}))
$k_{//}$ c/ω_{pp}
(b)
$\times 10^{-7}$
-0.815 < ω/Ω_{cp} < -0.752
Power (B_0^2/d($k_{//}$ c/ω_{pp}))
$k_{//}$ c/ω_{pp}

Figure 5.

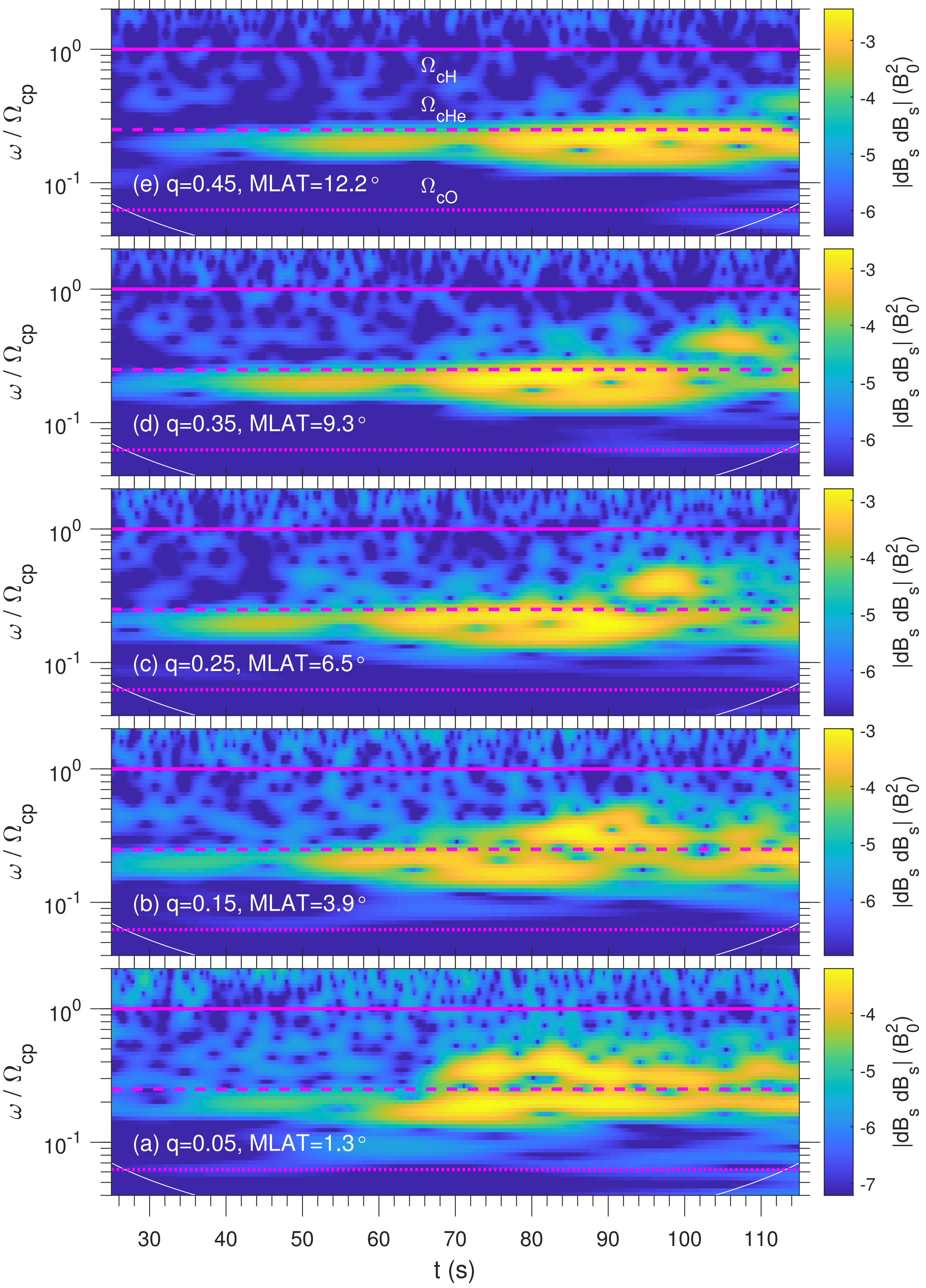

(e) q=0.45, MLAT=12.2°
(d) q=0.35, MLAT=9.3°
(c) q=0.25, MLAT=6.5°
(b) q=0.15, MLAT=3.9°
(a) q=0.05, MLAT=1.3°
Ω_{cH}
Ω_{cHe}
Ω_{cO}
ω / Ω_{cp}
$|dB_s\, dB_s|\ (B_0^2)$
t (s)

Figure 6.

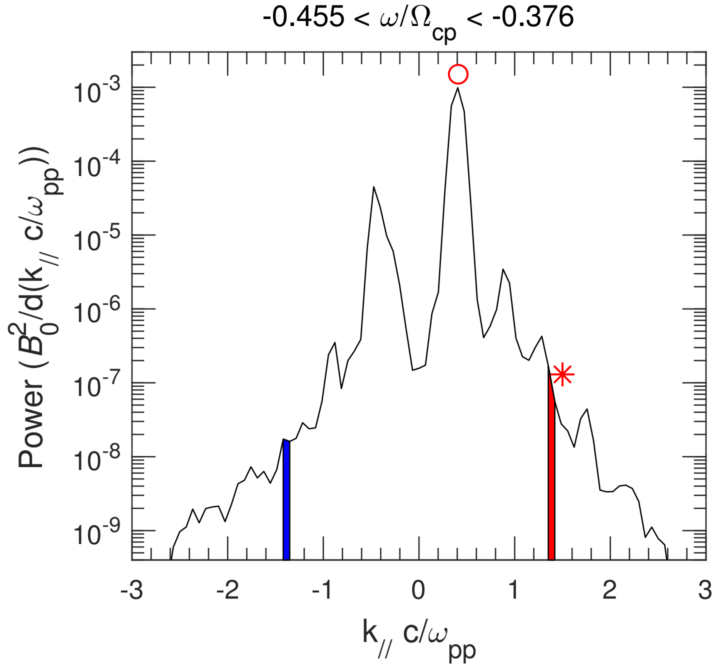

$-0.455 < \omega/\Omega_{cp} < -0.376$
Power ($B_0^2/d(k_{//}\ c/\omega_{pp})$)
10^{-3}
10^{-4}
10^{-5}
10^{-6}
10^{-7}
10^{-8}
10^{-9}
-3
-2
-1
0
1
2
3
$k_{//}\ c/\omega_{pp}$

Figure 7.

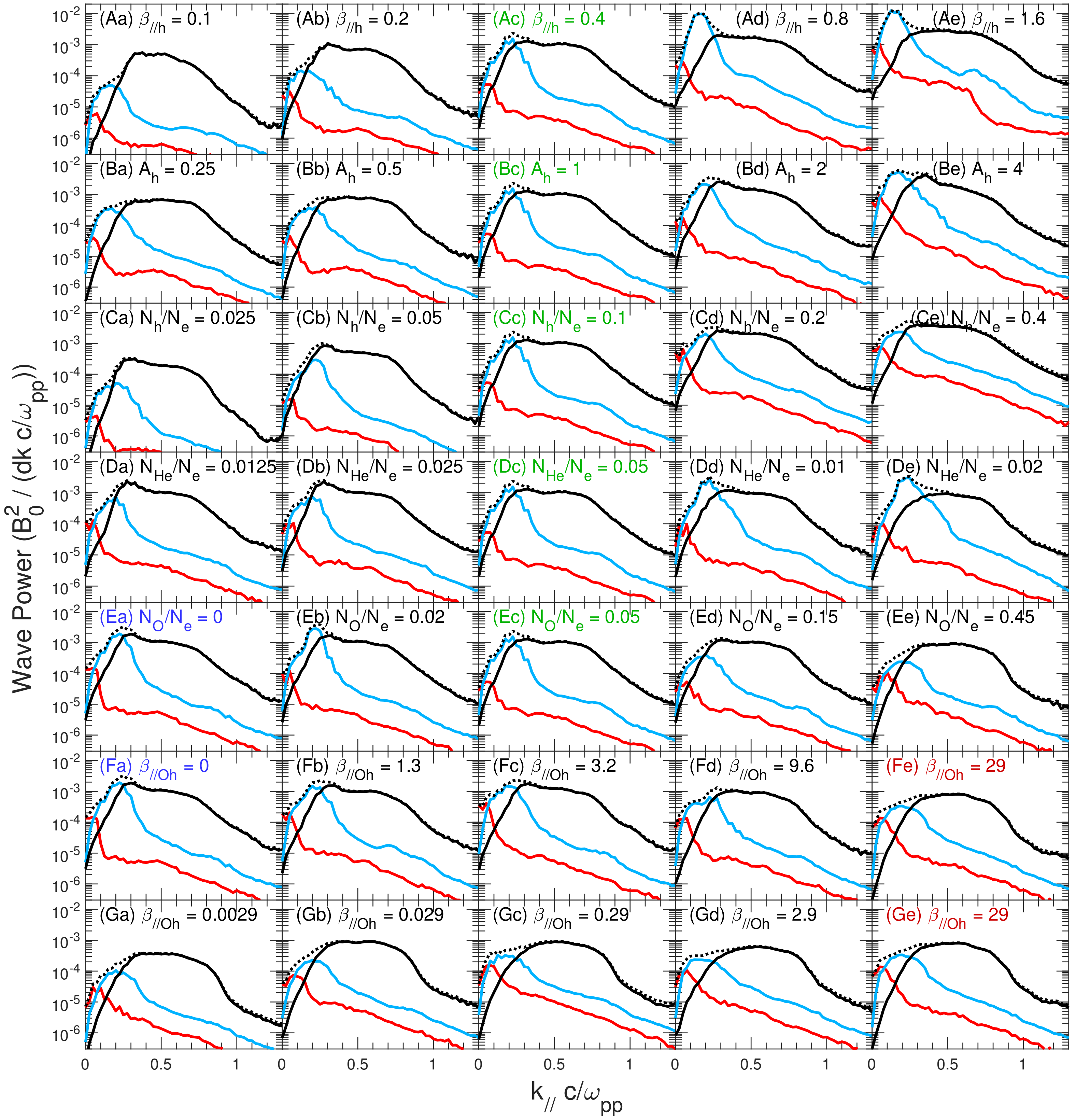

(Aa) $\beta_{//h}$ = 0.1
(Ab) $\beta_{//h}$ = 0.2
(Ac) $\beta_{//h}$ = 0.4
(Ad) $\beta_{//h}$ = 0.8
(Ae) $\beta_{//h}$ = 1.6
(Ba) A_h = 0.25
(Bb) A_h = 0.5
(Bc) A_h = 1
(Bd) A_h = 2
(Be) A_h = 4
(Ca) N_h/N_e = 0.025
(Cb) N_h/N_e = 0.05
(Cc) N_h/N_e = 0.1
(Cd) N_h/N_e = 0.2
(Ce) N_h/N_e = 0.4
(Da) N_{He}/N_e = 0.0125
(Db) N_{He}/N_e = 0.025
(Dc) N_{He}/N_e = 0.05
(Dd) N_{He}/N_e = 0.01
(De) N_{He}/N_e = 0.02
(Ea) N_O/N_e = 0
(Eb) N_O/N_e = 0.02
(Ec) N_O/N_e = 0.05
(Ed) N_O/N_e = 0.15
(Ee) N_O/N_e = 0.45
(Fa) $\beta_{//Oh}$ = 0
(Fb) $\beta_{//Oh}$ = 1.3
(Fc) $\beta_{//Oh}$ = 3.2
(Fd) $\beta_{//Oh}$ = 9.6
(Fe) $\beta_{//Oh}$ = 29
(Ga) $\beta_{//Oh}$ = 0.0029
(Gb) $\beta_{//Oh}$ = 0.029
(Gc) $\beta_{//Oh}$ = 0.29
(Gd) $\beta_{//Oh}$ = 2.9
(Ge) $\beta_{//Oh}$ = 29
Wave Power $(B_0^2 / (dk\ c/\omega_{pp}))$
$k_{//}\ c/\omega_{pp}$